Wound-Field Synchronous Machine-System Integration toward 8X Power Density and Commercialization

DOE Award # : DE-EE0008869

Final Scientific/Technical Report

Dr. Lakshmi Varaha Iyer
Magna International Inc.
750 Tower Drive
Troy, Michigan, USA 48098

1. EXECUTIVE SUMMARY

In support of VTO's Electric Drive R&D activity, the Electric Drive Technologies (EDT) Consortium, a multi-disciplinary team of national labs and universities, coordinates and conducts a portfolio of research to advance the state-of-the-art in electric drive technologies. The Consortium established the following strategic goal listed below:

EDT Research Consortium Strategic Goal (compared to 2015 baseline)

A 125kW electric traction drive system:

- 8X power density improvement, or 1/10 the volume (33 kW/L)
- ½ the cost ($3.3/kW)
- 2X useful life (300,000 miles)
- 100 kW/L inverter and a <20,000 rpm, 50kW/L electric motor

The objective of this project is to design a Wound Field Synchronous Machine (WFSM) with 8X power density improvement and cost below $3.3/kW.

The approach includes modeling, design optimization, prototype development and hardware testing of wound field synchronous machine, cooling system, and wireless power transfer technology. The project is divided into three budget periods outlined below:

- Budget Period 1 – Simulation to determine the feasibility of achieving goal and concept design.
- Budget Period 2 – Design motor for build and prototype rotor excitation system
- Budget Period 3 – Build and test motor relative to project goals

This project and proposed wound field synchronous machine technologies are attractive due to the following:

- An 8x increase in power density provides significant weight and packaging benefits to the powertrain leading to increased EV driving range.
- Motor does not use magnets of any kind. Only uses copper and steel as active materials.
- Through the removal of rare earth permanent magnets, reduced concerns over environmental footprint and commercial availability.
- High power factor through field excitation control, reducing the required size of the main traction inverter (IPMSMs and IMs).
- Direct field weakening and large constant power speed range (CPSR) through field excitation control.
- Potential for improved safety through field control during inverter fault conditions (IPMSMs)

This project report details various tasks carried out in the project such as:

- Magneto-structural design optimization of wound field synchronous motor and prototype build
- Rotor excitation system design, build and testing.
- Cooling system design and simulation
- Test setup development and hardware testing

2. MAGNETO-STRUCTURAL DESIGN OPTIMIZATION OF WOUND FIELD SYNCHRONOUS MOTOR AND PROTOTYPE BUILD

1) Development of Optimization Tools for WFSM Prototypes

Tools for the design of traction wound field synchronous machines (WFSMs) were refined and developed over the course of this project. Initial design studies were carried out using WFSM design tools originally developed by the Illinois Institute of Technology (IIT) for other projects. These design tools utilized the free and open-source FEMM software as the finite element solver. FEMM was controlled through extensive MATLAB scripting to automatically create geometries, set up simulations, and post-process the results. To reduce the computational time of optimizations the MATLAB Parallel Toolbox was used to create a series of parallelized magneto-static simulations either of different rotor positions for the same design or of different designs. In this project, refinements of existing geometric templates were carried out to study different distributed/concentrated fractional slot pole combinations. Examples of some of the geometric template topologies are shown in Fig. 2.1. Thermal modeling of specific designs was carried out by exporting the geometry and materials information to MotorCAD.

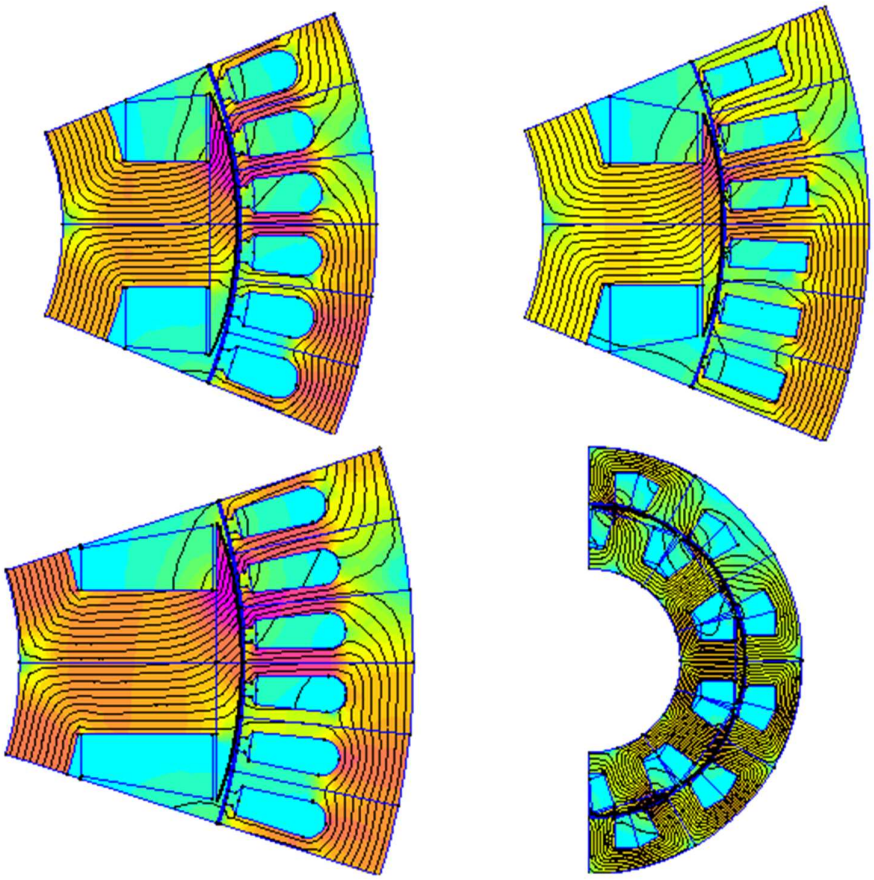

Fig. 2.1. Representative WFSM geometric templates from IIT's in-house FEMM/Matlab optimization suite.

Direct multi-objective optimizations were carried out using a differential evolution algorithm to vary machine geometric and loading parameters and find the best trade-off

between electromagnetic torque and machine losses subject to constraints such as torque ripple, voltage ripple, stator current density, field current density, etc. During design optimization runs up to ~48,000 designs were evaluated for a slot/pole combination and winding technology (e.g. hairpin versus random winding). Pareto fronts of the designs with the best trade-offs between torque production and losses were used for comparison of different slot pole combinations, winding technologies, assumed slot files, etc. A representative example of the comparison between Pareto fronts is shown in Fig. 2.2 for peak torque output at the corner speed. For these particular optimizations the target torque was 275 Nm. The different symbols correspond to different slot pole combinations, winding technologies, assumed slot fills, etc.

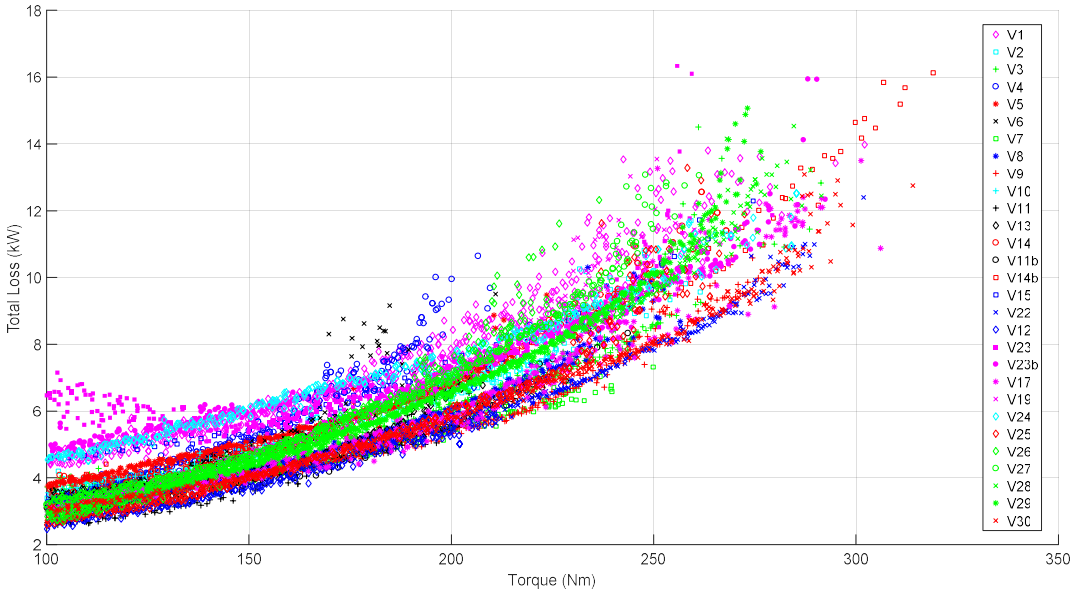

Fig. 2.2. Summary of direct optimization Pareto fronts. The different symbols and versions in the legend correspond to different slot pole combinations, winding technologies, assumed slot fills, etc.

Typically, only a single operating point, such as the peak torque at the corner speed, was evaluated for each design. To evaluate multiple operating points needed for drive cycle analysis was computationally infeasible even with a large number of CPUS (e.g., 16 CPU cores) executing FEMM simulations in parallel. The overall drive cycle efficiency and its comparison to the drive cycle efficiency of state-of-the art and upcoming production interior permanent magnet synchronous machines (IPMSMs) was a critical evaluation metric. The computational expense of evaluating a WFSM design is higher than a permanent magnet synchronous machine (PMSM) design because of the WFSMs variable field excitation. To make the drive cycle optimization computationally feasible an alternative metamodeling-based optimization approach was developed instead.

Meta-modeling-based optimization utilizes two stages. In the first stage the design space is sampled. In this case each sample corresponds to a specific WFSM design. Each design is evaluated at a number of operating points. In this project, typically between 10 and 16 operating points were evaluated for a given design. A metamodel which predicts outputs such as the weighted efficiency of drive cycle operating points or field winding ohmic loss is constructed as a function of input geometric and excitation variables. The construction of the metamodel can be thought of as response surface modeling, but more advanced fitting functions can be used than the polynomial functions typically used in the design of experiments response surface

modeling as shown in Fig. 2.3. Using a metamodel saves computational time from two perspectives. The sampling to form the metamodel, uses many fewer samples than a direct optimization. For this project, the number of design samples to construct a metamodel would regularly be between 500 and 2000 designs. Instead of directly calling the finite element solver to evaluate a potential design during the optimization, the metamodel is called instead. This is typically orders-of-magnitude faster than directly evaluating designs during the optimization process. Once the optimization has reached its stop criteria the selected design or designs from the Pareto front can be simulated using finite elements and the metamodel predicted outputs validated. Once the metamodel is constructed multiple optimizations can be run or tweaked very quickly. This is a major advantage compared to direct optimization where if the optimization inputs, objective function(s), or constraints are changed an entirely new optimization must be started from scratch.

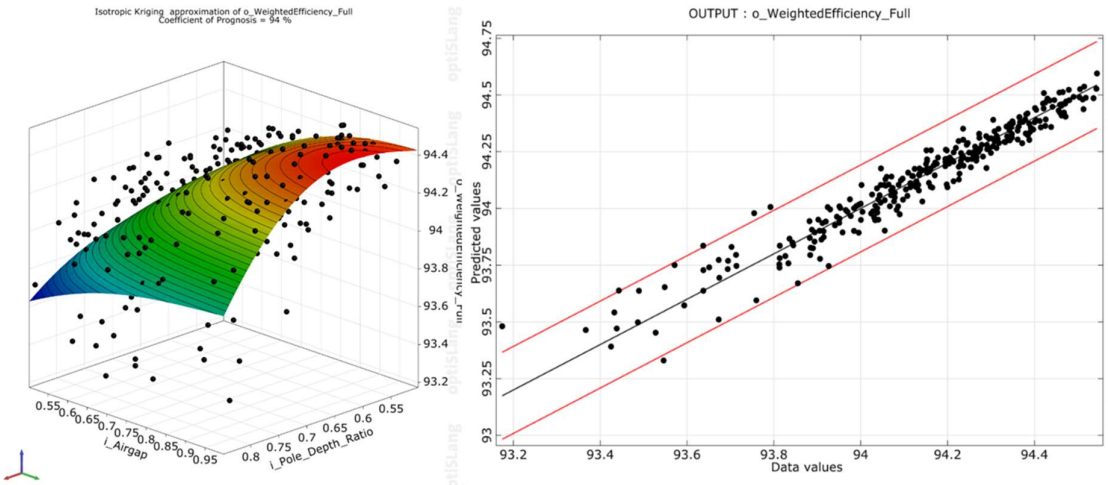

Fig 2.3. Representative example of (a) metamodel surface of weighted efficiency shown for two inputs, airgap thickness and pole depth ratio while all other inputs are held at the midpoint of their ranges, and (b) comparison of the finite element predicted and metamodel predicted values of the weighted efficiency. In this example 300 sample designs, indicated by dots, were used to construct the metamodel.

To implement the metamodeling based WFSM optimization extensive Python scripting was used to link ANSYS OptiSlang and ANSYS MotorCAD. ANSYS OptiSlang was used as the metamodel sampling and creation tool. ANSYS MotorCAD was used for the WFSM design finite element evaluations. Both the electromagnetic and structural behavior of WFSM designs were evaluated in ANSYS MotorCAD. To further reduce the computational time Python scripting was used to control multiple instances of MotorCAD and evaluate multiple designs in parallel (usually 8 but up to 10 was possible).

The Python scripting included the capability to create custom rotor geometries for a more accurate structural evaluation including adding fillets to the field winding window. The scripting was also flexible in terms of fixing the stator geometry to match an existing stator, or including it in the optimization, and the type of winding technology used, for example hairpin versus random distributed windings. Outputs from the finite element evaluation of each operating point include torque, torque ripple, losses including full FEA evaluation of the stator AC loss, maximum stress, terminal voltage and ripple, equivalent circuit parameters, etc. The

outputs were transmitted back to ANSYS OptiSlang and also saved as a spreadsheet for each design.

2) Design of WFSM Prototypes

A large number of potential WFSM design variants were optimized for different slot pole combinations, stator winding technologies (random versus hairpin), field slot fills, and corner speeds to achieve a power density of 50 kW/L. A representative optimized cross-section for a fully custom WFSM with hairpin stator is shown in Fig. 2.4. An example of a small subset of the WFSM topologies examined in metamodeling-based drive cycle optimizations are shown in Fig. 2.5. The custom rotor geometry in Fig. 2.4 is plainly visible compared to the default ANSYS MotorCAD geometric templates visible in Fig. 5. In Fig. 2.5 custom rotor geometry DXF imports are overlaid as the green lines.

To minimize the overall capital expenditure for potential serial production it was decided to use an existing serial production hairpin stator available to Magna International with a custom-designed rotor. A final set of operating points that are derived from an internal Magna drive cycle were selected. The operating points and torque speed envelope were selected for a minimum battery voltage of 325 V_{dc}. The torque speed plane envelope is shown in Fig. 2.6. A nominal voltage of 400 V_{dc} and increased corner speed was set for the peak power density point for evaluation if the design reached the 50 kW/L design goal.

WFSM rotors were optimized corresponding to the operating points contained within the torque speed envelope of Fig. 2.6. Rotors were designed assuming a high field winding slot fill was achievable using rectangular profile conductors.

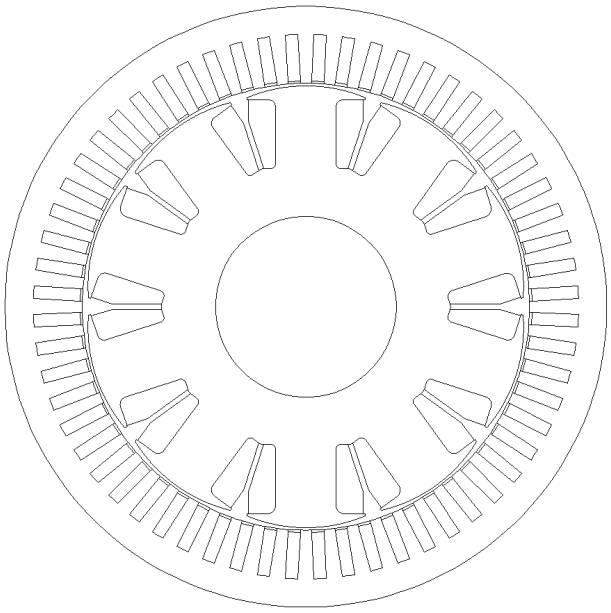

Fig. 2.4. Representative cross-section of optimized wound field synchronous machine

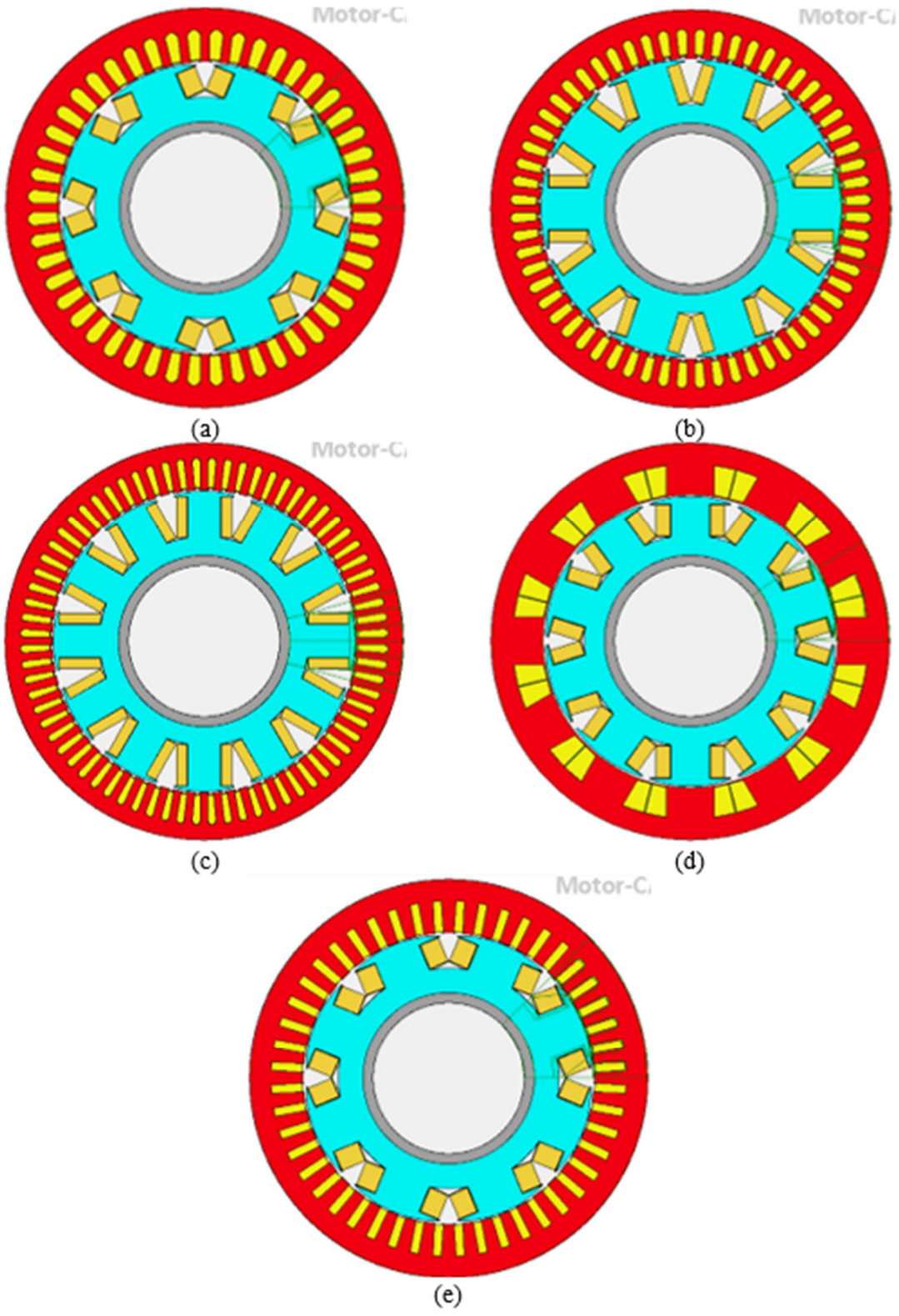

Fig. 2.5. Representative sample of WFSM topologies examined in metamodeling-based drive cycle efficiency optimizations.

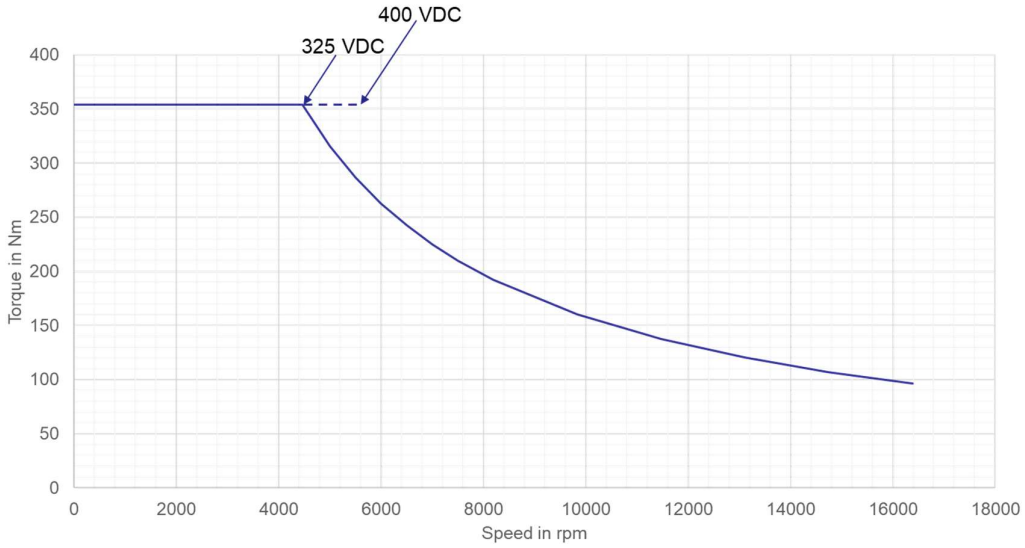

Fig. 2.6. Torque speed envelope for final WFSM design optimizations.

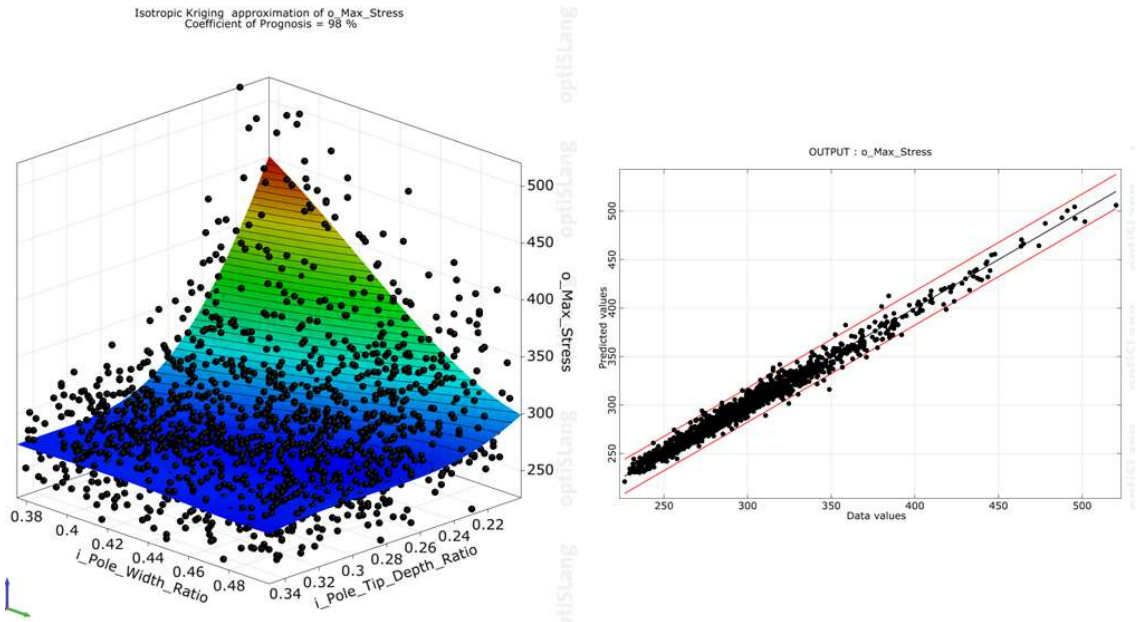

Fig. 2.7. Representative weighted efficiency metamodel surface for sampled designs indicated by black dots for two input parameters (right) and comparison between actual and predicted values (left).

Overall, the electromagnetic performance was evaluated at 10 operating points for each design in the metamodeling sampling and construction process. Additionally, the maximum Von Mises stress in the rotor lamination was calculated for a 20% overspeed condition for two scenarios. In the first scenario the mass of the end turns is not considered and is assumed to be supported by the end caps. In the second scenario the entire estimated mass of the end turns is supported by the lamination pole caps with none of their mass being supported by the end caps. The true maximum Von Mises stress is likely bounded by these two scenarios. The Von Mises stress simulations were carried out in in ANSYS MotorCAD which only has 2D linear solver capabilities and limited boundary conditions. Full 3D stress analysis was carried out once the

design of the endcaps was completed. To carry out the metamodeling-based optimization process more than 1500 design samples were used to construct the metamodels for each WFSM rotor variant. An example of the maximum Von Mises Stress meta-model is shown in Fig. 2.7 along with the sample designs.

Considerable time was invested in the mechanical design of the optimized rotor variants to ensure manufacturability and compatibility with the dynamometer available for testing. The most critical design element are the pole caps as they determine the "windability" of the field winding and the retention of the field winding at high speeds. The rotor assembly was also designed to be able to swap between two types of field excitation systems, brushes and slip rings, and a high-frequency rotating transformer. Representative rotor assembly is shown in Fig. 2.8.

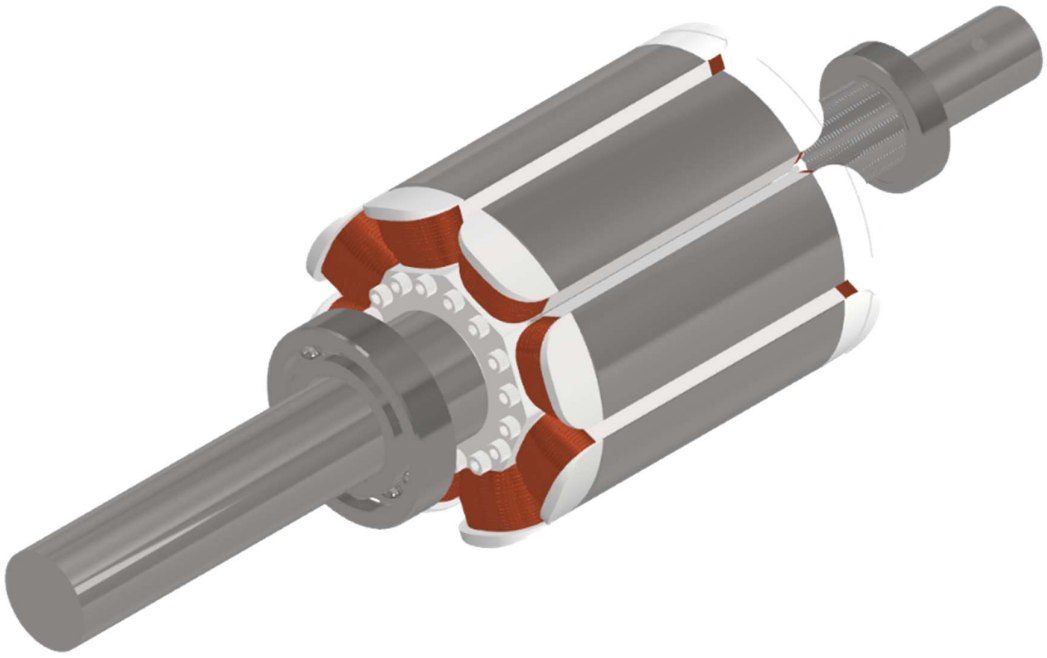

Fig. 2.8. Representative rotor assembly. The banding, aeroshell inserts, and excitation system are not shown.

Summary of final prototype design:

- 70% slot fill factor in the rotor, 640 A rms/phase maximum current, 210kW peak power
- Motor design optimized for a hairpin stator in serial production
- Combined magnetic and structural optimization
  - Maximize weighted efficiency subject to current density, torque ripple, voltage, and Von Mises stress constraints
- New operating space map with 10 load points
- Designed to achieve a 50 kW/L active power density
  - Design can reach this power density
- Predicted weighted efficiency of the machine 95.89%
  - Includes full stator DC+AC ohmic loss, field ohmic loss, and all iron losses

3) Construction of WFSM Prototypes

WFSM prototypes were constructed during the final phase of this project, one for testing and one for back-up. Both prototypes used a serial production hairpin stator with 8 poles. The rectangular rotor winding profile allows for a high slot fill field winding. The downside of the rectangular profile winding is that it is more expensive and requires a custom winding machine (Generally needle winding machine nozzles are used with round wire). A second prototype used standard round profile magnet wire. The two slot fills and conductor profiles require different winding technologies and construction processes. Even trying to maintain an orthocyclic pattern for the winding results in a lower slot fill than using the rectangular profile wire. The advantage of the using the round magnet wire for the winding is the lower cost of the magnet wire and the ability to use winding machinery with minimum modifications (e.g., needle winding machines). Because of the lower slot fill the round wire field winding is more difficult to cool.

A serial production hairpin stator, Fig. 2.9, was used as the common stator for both prototypes to minimize the capital expenditures to develop a new custom hairpin stator for the WFSM design. Even at prototype scales the costs for a custom hairpin stator are large. The compromise with using an off-the-shelf in production stator is that the potential performance gains of using a custom stator are not available. The serial production stator was available and most closely fit the desired packaging size/terminal voltage requirements for the WFSM prototypes. While using a larger number of hairpin conductors in a slot would have been preferable for the WFSM prototypes to reduce the stator AC loss it is not as critical as in an interior permanent magnet synchronous machine. This is due to the variable field excitation which is reduced during field weakening at high speeds/high frequencies. The field excitation magnitude is only one contributor to the stator AC loss but the reduction in the field excitation does help to manage the stator AC loss at high speeds.

The overall mechanical design of both WFSM prototypes was very similar. Two cooling approaches were used simultaneously in the WFSM prototypes, a water-ethylene-glycol (WEG) cooling jacket and spray/jets of automatic transmission fluid (ATF) at the end turns of the field winding. Two field excitation methods were also to be used one at a time, brushes and slip rings, and an inductive power coupler (originally a capacitive power coupler). As the WFSM prototypes are for dynamometer testing of the power conversion performance and not integration into an actual vehicle drive train the packaging of the WFSM prototypes was designed for flexibility in experimental investigation. An overview of the exterior mechanical package is shown in Fig. 2.10.

The stator core was housed in a two-part shell with a spiral water-ethylene-glycol (WEG) cooling jacket. The inner shell which has the WEG directing channels machined into its surfaces was first heat shrunk over the stator core. The outer shell which seals the WEG channels was then shrunk over the inner shell and stator core. The final stator assembly with the stator core and cooling jacket is shown in Fig. 2.11.

Wound rotor before banding and varnishing is shown in Fig. 2.12. Final rotor with shaft and slip rings is shown in Fig. 2.13. The interpolar aeroshells and winding retention features are visible between poles. Fig. 2.14 shows the stator and rotor assembled into the jacket and casing. Fig. 2.15 shows the complete prototype from the driving and non-driving end.

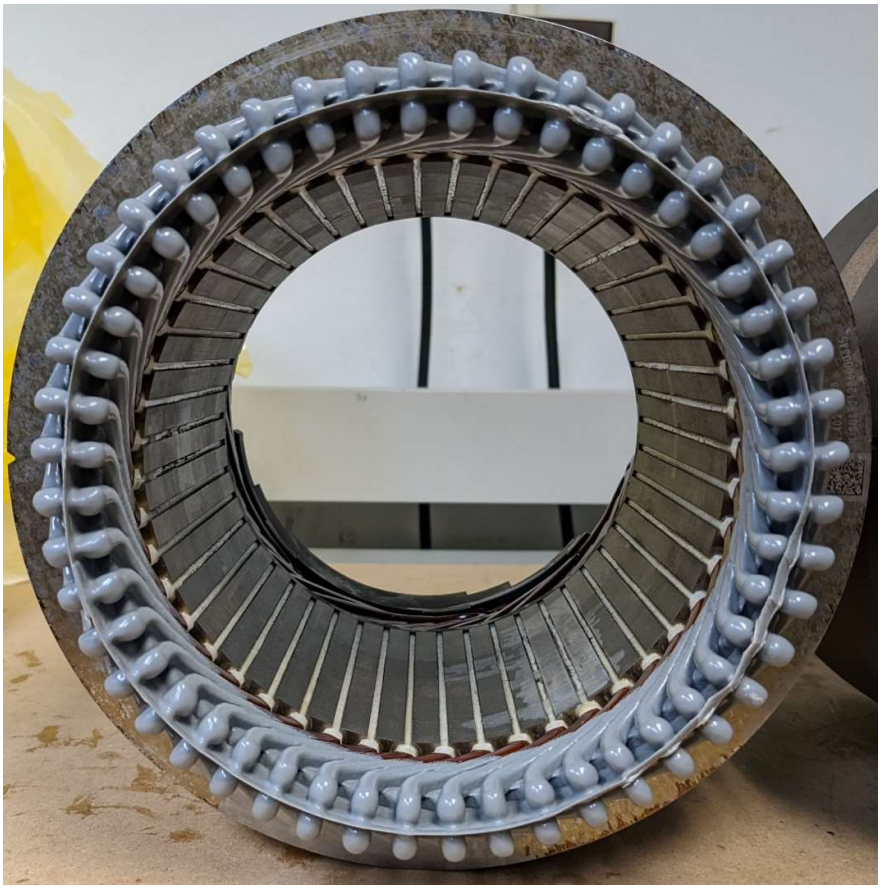

Fig. 2.9. Serial production hairpin stator used in WFSM prototypes.

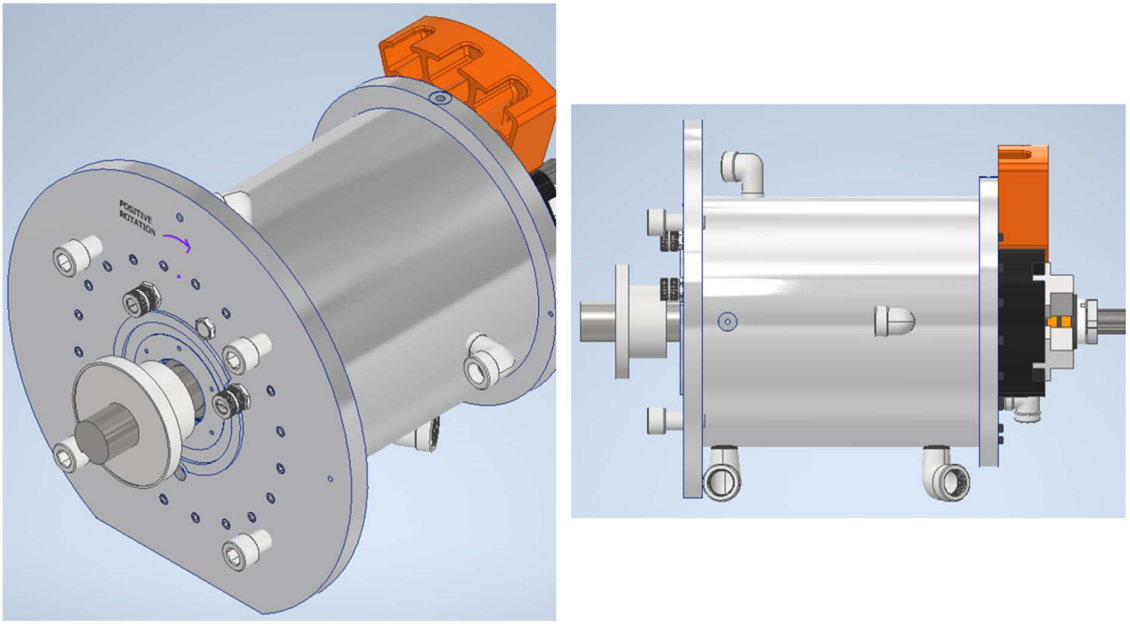

Fig. 2.10. Overall exterior view of the mechanical package for dynamometer testing of the WFSM prototypes.

Fig. 2.11. Final assembly of the stator with stator core and jacket.

Fig. 2.12. Wound rotor before banding and varnishing

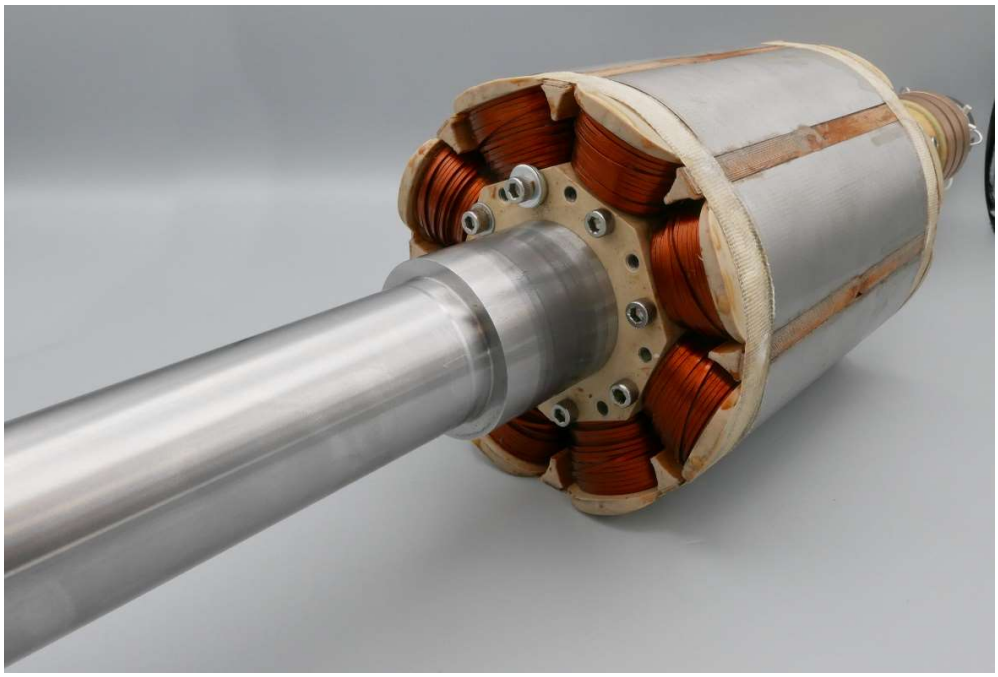

(a)

(b)

Fig. 2.13. Final rotor with shaft and slip rings.

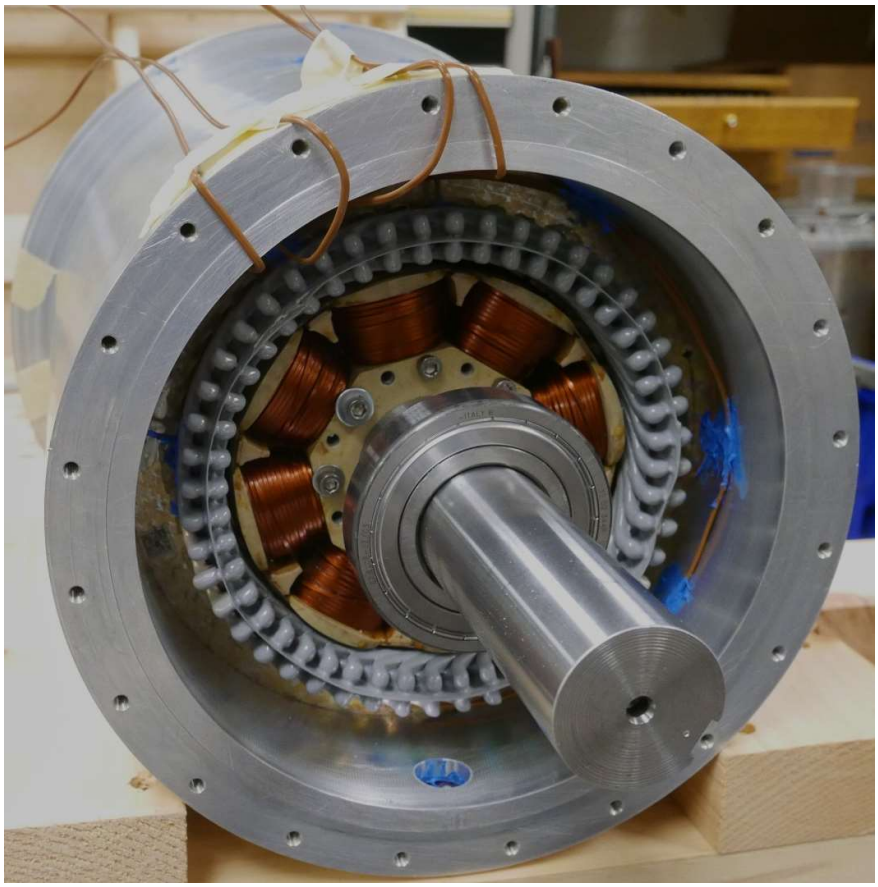

Fig. 2.14. Stator and rotor assembled into the jacket and casing.

(a)

(b)

Fig. 2.15. Completed prototype. (a) Non-driving end view. (b) Driving end view.

3. ROTOR EXCITATION SYSTEM DESIGN, BUILD AND TESTING

The objective of the excitation system for this project was to be brushless and low cost. Brushless operation is required for machine longevity at high speed and the cost of the system should not exceed the permanent magnets it seeks to replace. Numerous magnetically coupled approaches have been demonstrated in the literature [1], but a capacitive power transfer (CPT) approach was identified as an opportunity given its low-cost materials [2]. The initial low field power requirement of ~1kW for the project was also ideal for CPT technology. However, as the project progressed, and the overall machine design was iterated, the final rotor field peak power requirement rose to 7kW. Existing CPT technologies rely on HF Band (3-30 MHz) wide bandgap (WBG) inverters and rectifiers, and at 7kW the necessary electronics and compensation networks were no longer practical. For reference, MHz, air-gapped CPT systems in the form of [3] appear to be competitive for applications < 2 kW [4]. Emerging double layer CPT systems may satisfy higher power level requirements in the future [5]. At this stage the team pivoted to an inductive power transfer (IPT) system in the form of a gapped rotary transformer approach following standard transformer design processes outlined in [6]. Fig. 3.1 shows the rotor excitation system fabricated and tested for the CPT system. Fig. 3.2 shows the CPT PCB stack visualized and designed to be mounted on the WFSM shaft.

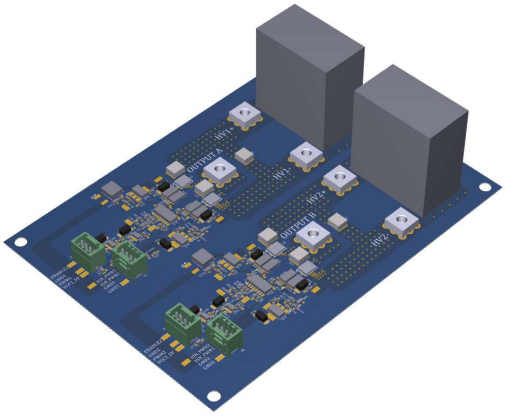

(a)

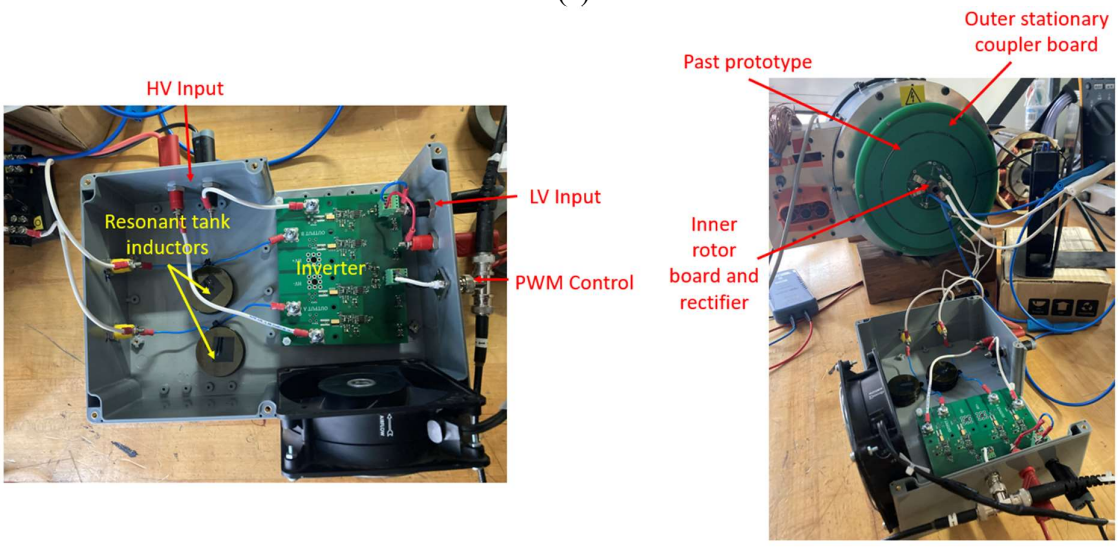

(b)

Fig. 3.1. (a) Initial rendering of the 6.78 MHz rotor inverter designed, fabricated and tested for he CPT system. (b) CPT based rotor excitation system fabricated and tested.

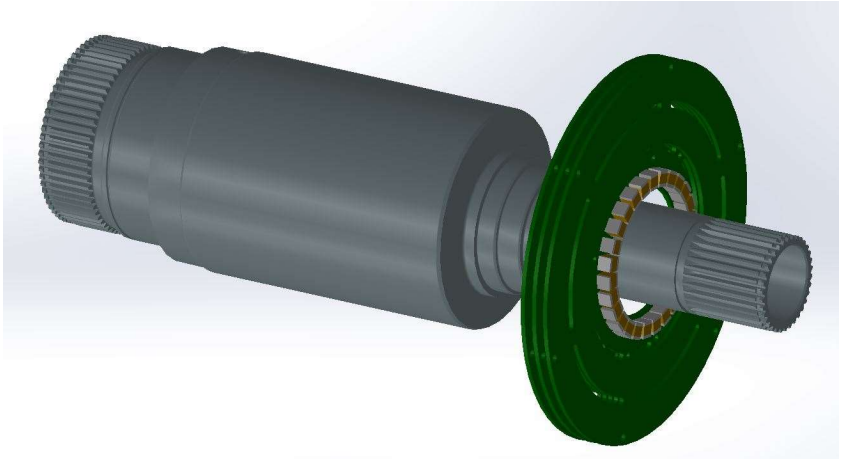

Fig. 3.2. CPT PCB stack visualized and designed to be mounted on the WFSM shaft.

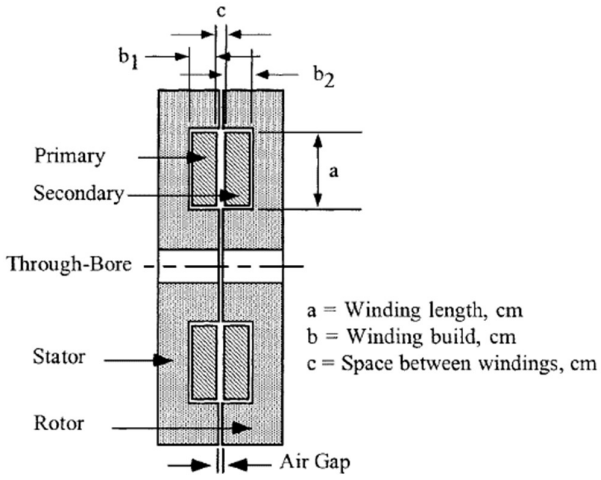

(a)

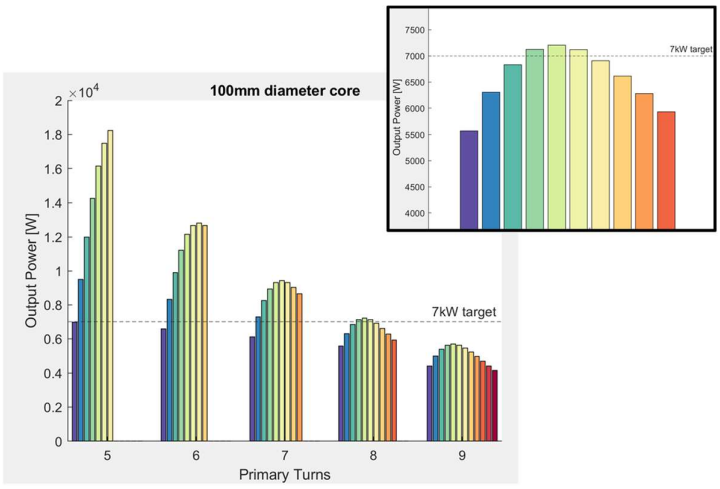

(b)

Fig. 3.3. Selecting transformer dimensional parameters and number of turns to meet 7kW [6]

An axial pot core geometry was chosen for the rotary transformer core. These cores are readily available from multiple sources, making them a good candidate for commercialization. The core dimensions were parameterized, then swept and evaluated both analytically and with finite element analysis to determine the optimal size and number of turns. Ultimately a 100mm diameter, 40mm axial length, transformer operating at 75kHz was designed to provide > 7kW of power transfer to the rotor. The transformer has an 8 turn primary and 12 turn secondary for a net gain of 1.5. The step-up ability of the transformer enables 7kW to be delivered to the field winding regardless of battery voltage level, i.e. 290V – 425V. The cross section of the transformer is outlined below in Fig. 3.3 along with finding the primary turns.

The selected core design was machined from ferrite blocks, pictured below. Note the two holes for the winding leads to exit the transformer core without interfering with the air gap. The selected wire was 14 AWG equivalent litz wire comprised of 5 bundles of 52 strands of 38 AWG wire. The coils were wound on a separate bobbin/mandrel and then slid off into the ferrite core and potted as shown in Fig. 3.4.

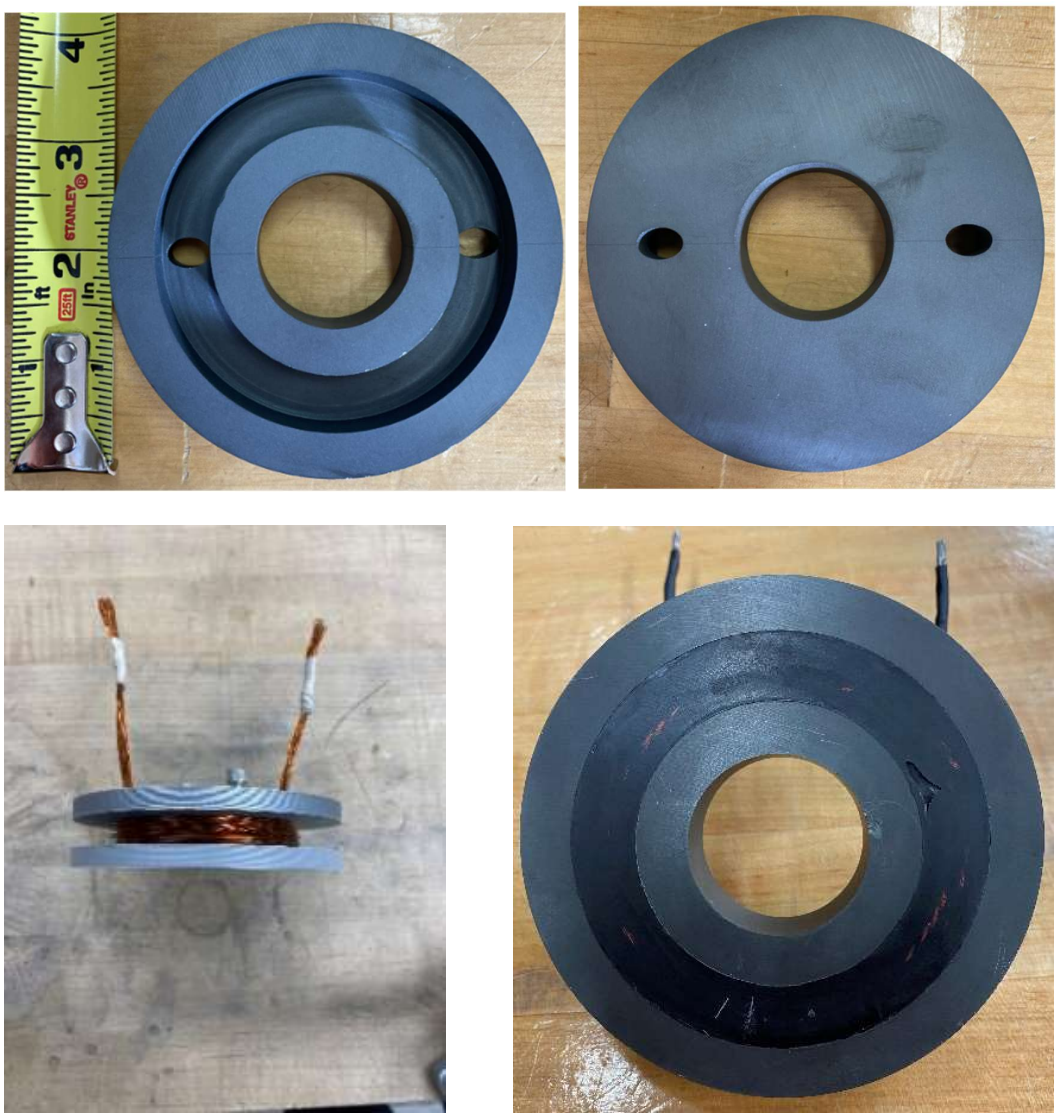

Fig. 3.4. Photos of IPT transformer cores, winding jig and potted final core assembly

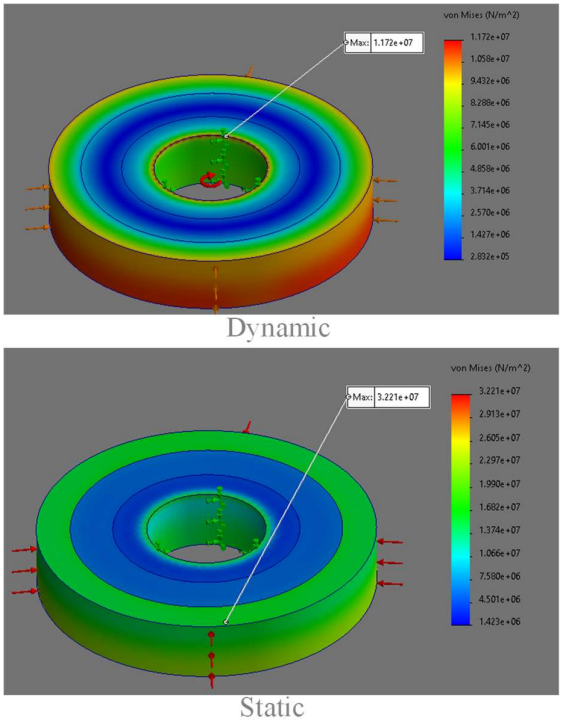

(a)

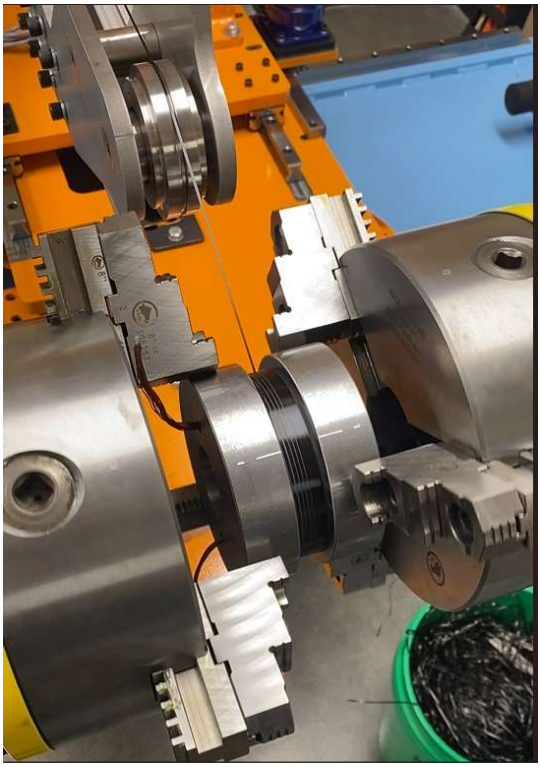

(b)

Fig. 3.5. (a) FEA of IPT system with a carbon fiber wrap. (b) Carbon fiber wrapping of IPT transformer core.

Since the core will rotate at high speeds, finite element analysis was conducted to ascertain the structural limits of the core at a speed of 20 krpm. Initial simulations revealed transformer core mechanical failure, ultimately leading to a carbon fiber wrapped approach, simulation results are shown in Fig. 3.5 (a). With a carbon fiber wrap, the core has a margin of safety of 1.7. Next, the actual transformer assembly was carbon fiber wrapped using the pictured jig in Fig. 3.5 (b).

An exploded view of the IPT system is pictured below in Fig. 3.6, with the real-life physical components beneath the CAD drawing. This configuration was shown on a square bench plate that allows for lab testing off of the machine mounting.

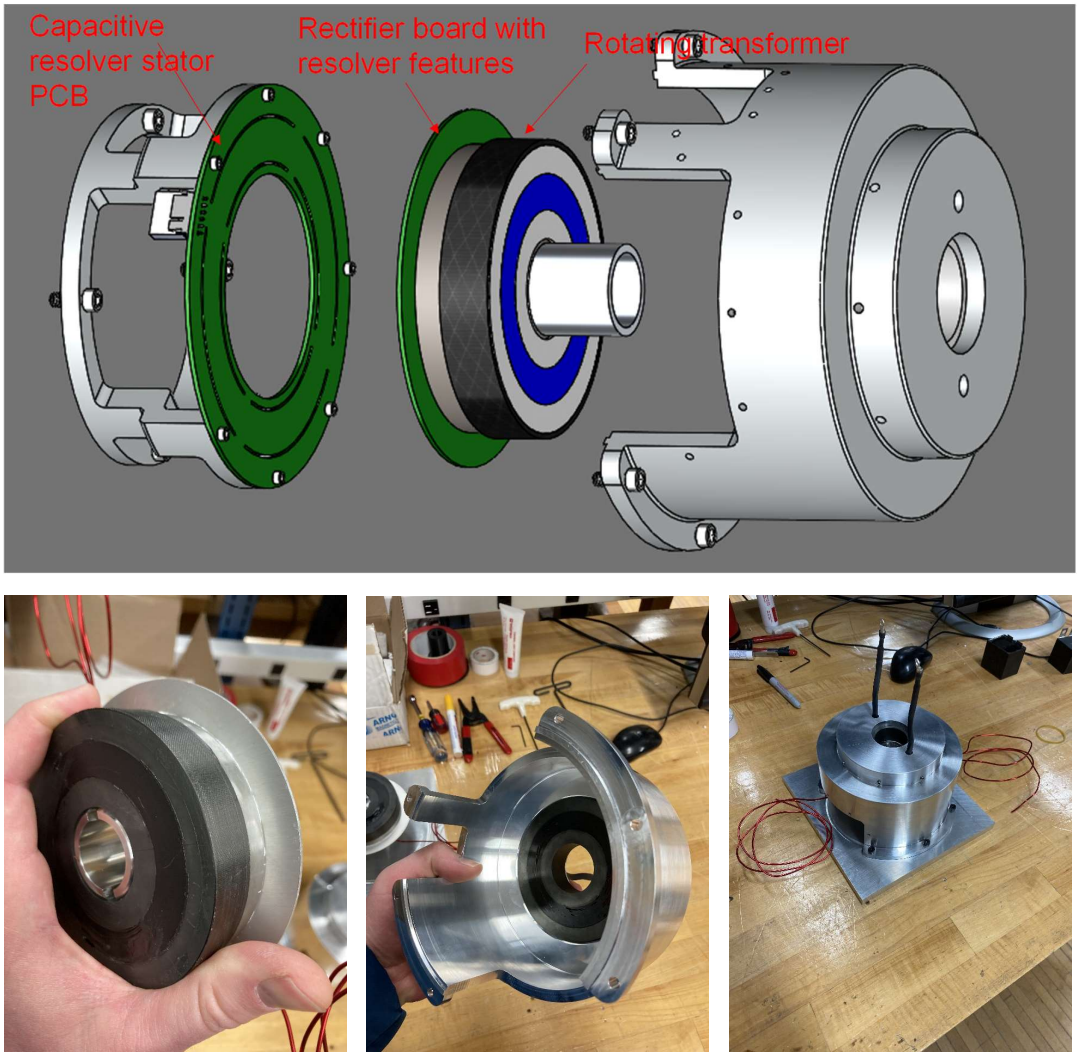

Fig. 3.6. Top – exploded CAD view of IPT system, Bottom – Carbon fiber wrapped rotor core, stator core embedded in aluminum housing, IPT components assembled on mock motor plate.

Alternatively, the IPT system is shown on the machine shaft in the Fig. 3.7 below to give a better idea of actual assembly. This view gives a better picture of the rotating rectifier. There are 8 SiC diodes, 2 parallel SiC diodes in each quadrant of a single phase bridge rectifier. The rotating diode board is an aluminum substrate board that provides superior thermal

performance for surface mount parts. The ability of the surface mount diodes to remain adhered (soldered) to the PCB at speed was verified using FEA.

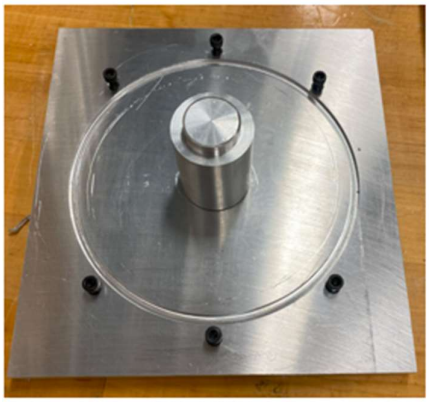

Test Plate.

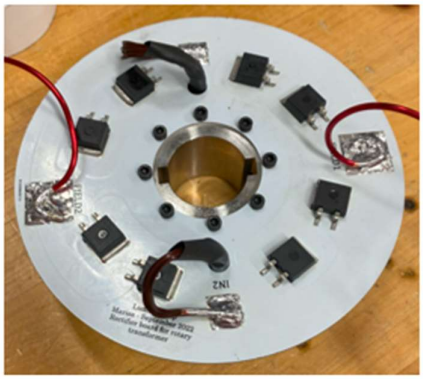

Rotor Rectifier Assembly.

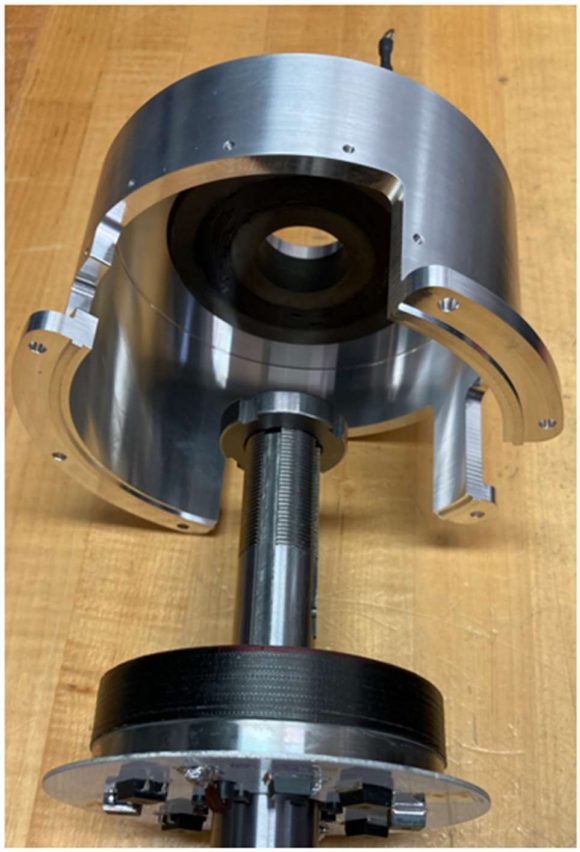

Exploded assembly.

Fig. 3.7. View of the rotating rectifier board and IPT assembly on the machine shaft.

Prior to bench testing, the measured transformer parameters were entered in a PLECS simulation to verify the transformer could safely and efficiently achieve 7 kW. The circuit for the simulation and lab testing is shown below in Fig. 3.8. Simulations predicted an overall system efficiency of 96% at 7kW with most of the losses occurring the transformer and diode rectifier. The simulated combined efficiency of the transformer and diode rectifier was 97.5 %, indicating that 175 W of heat will need to be dissipated during peak operation.

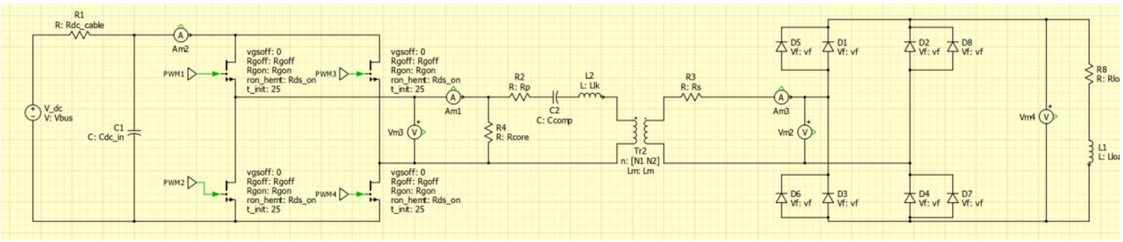

Fig. 3.8. Schematic for circuit simulations and bench testing of IPT system

Benchtop electrical testing was done while stationary such that load voltages, currents and temperatures could be measured directly without slip rings or radio telemetry. Fig. 3.9 (a)

shows the test setup. A 500 mH inductor along with multiple space heaters connected in parallel form the equivalent rotor load. To represent the worst scenario, testing was performed with the lowest inverter DC link voltage, 290V, which will yield the highest current to achieve 7 kW. Testing was done in 30 second bursts and then the set up could cool down between tests. During the 7 kW test a maximum temperature rise of 50 C above ambient was observed through thermocouples placed in the transformer and diode assemblies. The measured efficiency of the transformer plus diode rectifier was ~97% at 7 kW, slightly below the predicted 97.5%, but overall very reasonable. The system efficiency (inverter, transformer, diode rectifier) was ~93% at 7 kW. The inverter used was a first generation SiC unit, nearly 10 years old, and we anticipate an additional 2-3% gain is possible with more recent technology. Power and efficiency are summarized in Fig. 3.9 (b) below.

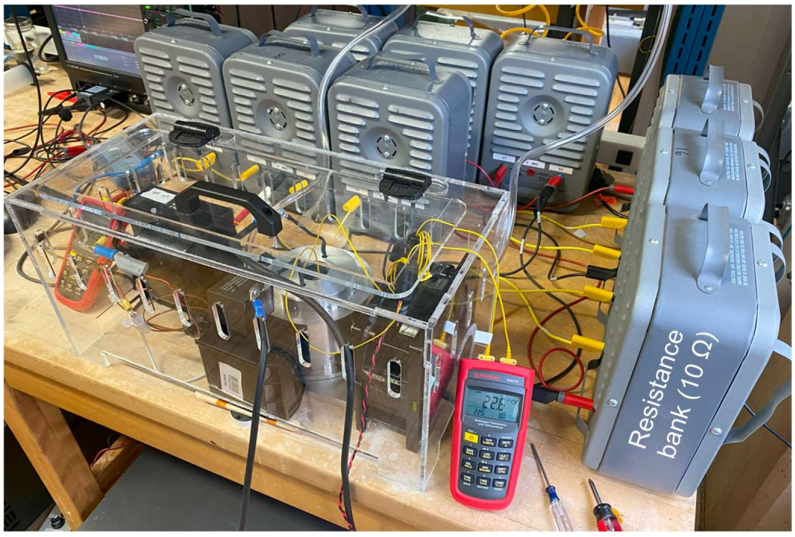

(a)

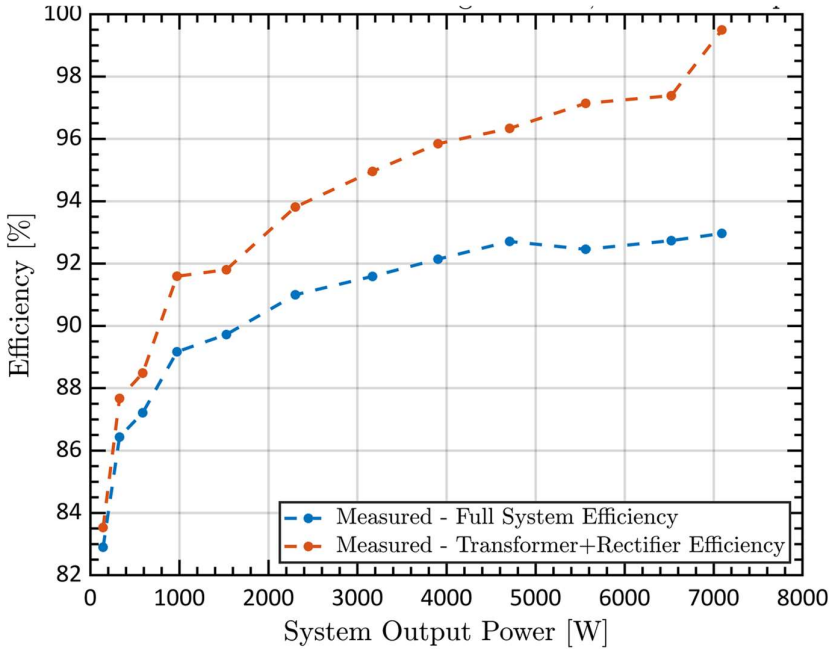

(b)

Fig. 3.9. (a) Bench test of IPT excitation system with dummy load. (b) Measured results

4. COOLING SYSTEM DESIGN AND SIMULATION

The objective is to design, optimize and test a WFSM motor thermal management system. This thermal management should efficiently cool the laminations and windings of the rotor and stator.

This report begins by outlining the key objectives and constraints imposed during the design process. Next, the preliminary designs of the WFSM motor's cooling system using simplified analytical tools like ANSYS Motor-CAD [7] are presented. Using MotorCAD, different cooling approaches such as cooling jackets [8- 11] or channel flows in the shaft [12, 13] can be studied. However, it should also be noted that although these conventional cooling solutions can reliably remove heat from stator windings, laminations and permanent magnets, the greater heat loads within rotor windings, remain a challenge to manage. A detailed schematic of the chosen cooling system, shown in Fig. 4.1, is then presented which includes direct jet cooling of the rotor windings to ensure the reliability of WFSM motor and indirect cooling using a cooling jacket for the stator. The flow fields and heat transfer characteristics of jets in rotational fields is a challenge to model computationally and have not yet been investigated in detail, therefore this report outlines the computational fluid dynamics (CFD) set-up of the cooling system. Experimental testing wraps up this report.

There are several objectives to be achieved in this project

1. Maintain maximum rotor temperatures below 180°C
2. Maintain maximum stator temperatures below 180°C
3. Reduce pumping power to the cooling systems
4. Reduce rotor drag losses

The constraints imposed include:

1. WEG temperature range (65-100°C)
2. ATF temperature range (65-100°C)
3. Max. WEG flow rate (10 L/min)
4. Max. ATF flow rate (10 L/min)

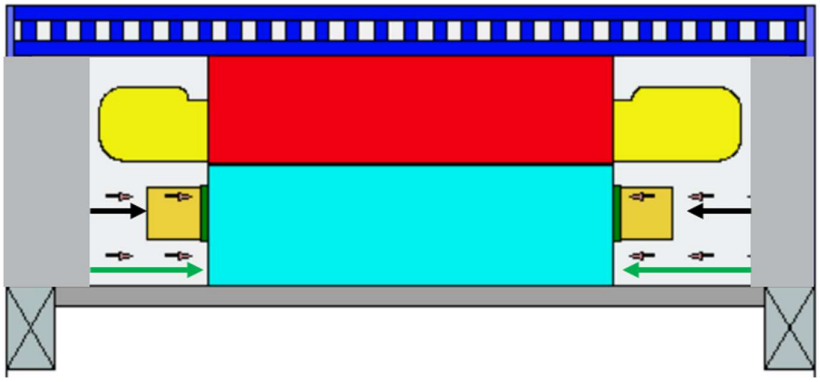

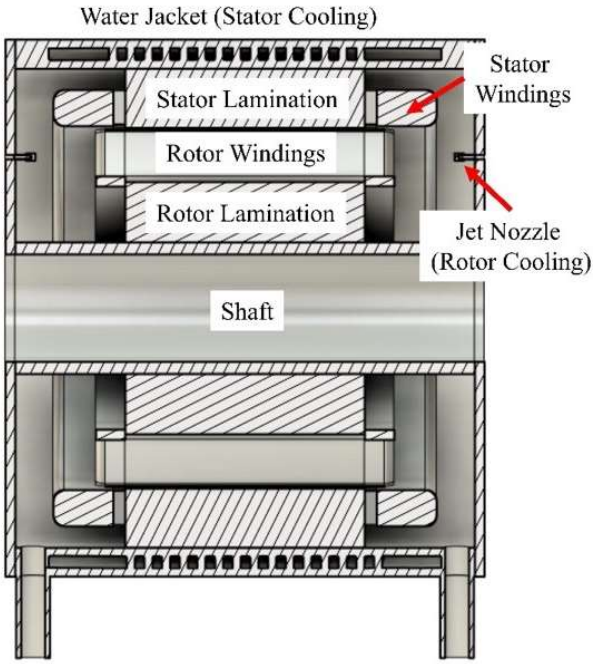

Fig. 4.1. General schematic of WFSM motor and cooling system architecture used in this project

Stator Jacket Cooling

Various cooling jackets were investigated as summarized in Table 4.1 and shown in Fig 4.2. All concepts presented are modifications of a serpentine design. As stated in the objectives, the optimal jacket would reduce stator winding and stator lamination temperatures while minimizing the pumping power or pressure drop required to pump the coolant through the jacket. Moreover, the cooling jacket should maintain cooling uniformity over the entire length of the motor (from front to rear end of the motor). In standard cooling jacket concepts, there is one inlet near the front of the motor and the outlet is near the rear of the motor [8-11]. With those standard cooling jackets, fresh fluid at low temperatures efficiently removes heat from the front of the motor, however as the fluid temperature rises as it travels across the length of the motor, a high temperature fluid near the rear of the motor cannot remove the same amount of heat, leading to a cooling nonuniformity of the motor. Therefore, the concepts considered for the stator jacket cooling aimed to eliminate the problem of cooling nonuniformity.

Jacket 1 introduced two inlets, one inlet at the front of the motor and one inlet at the rear of the motor. Two outlets are then present within the active region of the motor. Introducing two inlets ensures fresh fluid at the desired inlet temperature is used to uniformly cool the front and rear of the motor. With Jacket 1, major hot spots are located in the active region of the machine, therefore Jacket 2 cools the active region of the machine directly after the front region of the motor is cooled. The fluid is then immediately sent to the rear of the motor. Jacket 2 resulted in a very large pressure drop, therefore the two inlet and two outlets

concept is introduced again in Jacket 3, however the inlets are brought closer to the active region of the motor.

Jackets 1, 2, and 3 were unable to reach the target stator temperature (less than 160 degC) primarily due to the low amount of mixing and turbulence that is present in the serpentine design. Therefore, Jacket 4, which is a spiral concept, was simulated. Due to narrower flow passages in this concept, there is enhanced mixing and turbulence which allows for the proper cooling to 99 deg C maximum stator temperatures. The pressure drop with Jacket 4 is relatively high compared to other concepts tested, however at 11 kPa it is within an acceptable range. Therefore, for the WFSM, spiral Jacket (4) was considered for stator cooling.

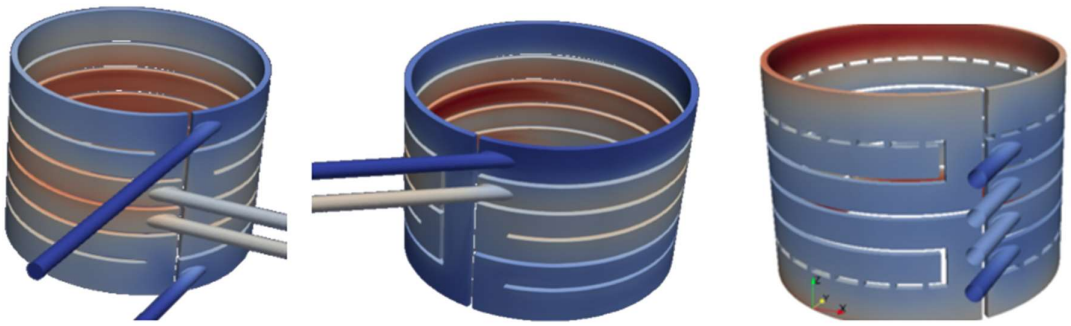

Jacket 1 Jacket 2 Jacket 3

Fig. 4.2. Different jacket architectures and computational results

Table 4.1. Cooling Jackets Investigated

Jacket	Max Temperature (C)	Pressure Drop (kPa)
1	173.0	5.5
2	137.0	17.7
3	185.0	3.45
4 (Spiral)	99.0	11.0

Rotor Jet Cooling

Due to complex modelling involved when computationally modelling rotating components, preliminary jet cooling concepts were investigated using Ansys MotorCAD. MotorCAD allows for the reduction of computational time, however at the expense of accuracy. Therefore, the design process is further carried out computationally after the preliminary MotorCAD phase.

MotorCAD employs a lumped parameter thermal network model (LPTN) which is developed using an electrical circuit analogy where temperature, heat flux and thermal resistance are analogous to voltage, current and electrical resistance, respectively. Each component of the WFSM motor where temperature is expected to be uniform is lumped together and represented as a node in the LPTN. At each node a value of temperature is to be determined [7]. Connecting each node are thermal resistances which emulate the heat flow

throughout each component of the WFSM motor. For electric motor design, the thermal resistances can be due to conduction, convection or radiation. In this work, radiation heat transfer can be ignored, therefore, the thermal resistance due to radiation is neglected. Thermal resistance values due to conduction depend on the geometry of various components of the motor and material properties. Finally, the thermal resistance due to convection is dependent on the heat transfer coefficient which is challenging to estimate for the jet cooling concept, which further demonstrates the need for computational methods.

Considering a fixed flow rate, if the number of jets is reduced greater cooling can be achieved. Therefore, initially a minimum number of jets was used for rotor cooling where the end windings and rotor lamination were directly impinged with jet fluid. In the MotorCAD model, multiple jets are used for the rotor end windings so that jet fluid can cover the front, top and bottom faces of the end windings. The spiral Jacket 4 from the previous stator jacket cooling studies was used for each MotorCAD simulation of the jet cooling. The stator jacket cooling was fixed with a WEG inlet temperature of 75 degC and flow rate of 8 L/min. For the jet cooling concepts, the oil inlet temperatures ranged from 75 to 100degC and the flow rate ranged from 1.6 to 12 L/min. Moreover, the nozzle diameters were fixed at 1.5 mm.

Preliminary MotorCAD simulation results are presented in Fig. 4.3 which represent the stator and rotor winding temperatures. Firstly, although the stator jacket cooling is fixed, the oil jet often splashes onto the stator windings, therefore there is some influence of the oil jets on the stator temperatures. It can be seen that in Fig. 4.3a, a decrease in oil inlet temperature and an increase in oil flow rate will reduce stator winding temperatures. The same trends can also be seen in Fig. 4.3b. Moreover, it can be seen that oil inlet temperature has a greater influence on stator winding temperatures compared to oil flow rate. Similar trends can be seen with the rotor winding temperatures in Fig. 4.3c and 4.3d. For all ranges of oil inlet temperatures and oil flow rates, the stator target temperatures were reached, however for oil temperatures greater than 100C, the target rotor temperatures could not be satisfied. To this end, the oil inlet temperatures were not to exceed 100C for the computational simulations to follow.

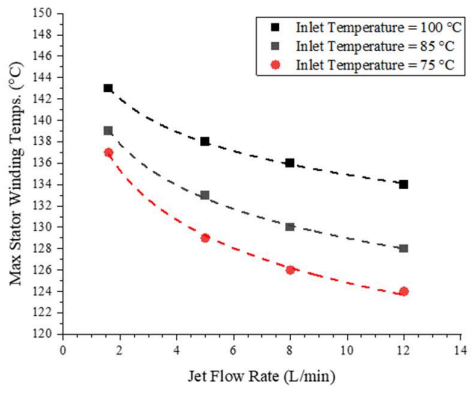

(a)

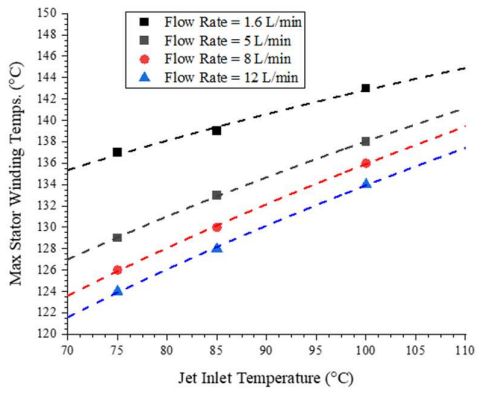

(b)

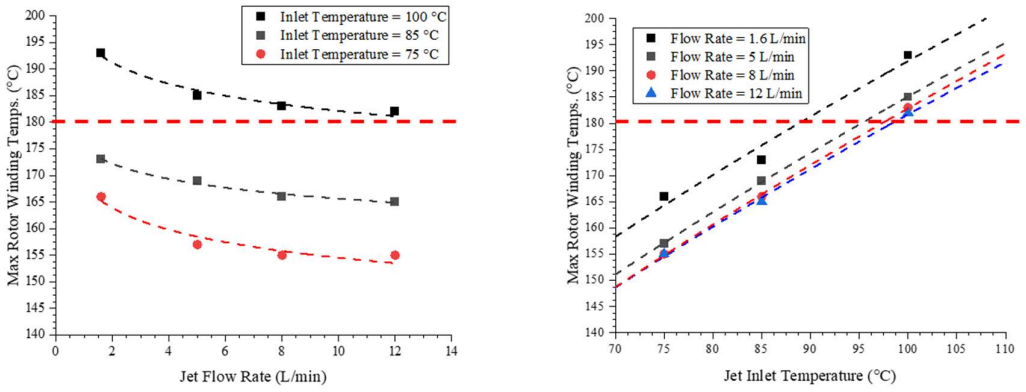

(c) (d)

Fig. 4.3. Stator and rotor winding temperature for various oil flow rates and oil inlet temperatures.

A CAD representation of the WFSM and casing is shown in Fig. 4.4 which is also considered as the computational domain for the numerical analysis. The computations consist of several computational domains such as the rotor lamination and rotor windings which rotate at a constant angular velocity. A cooling jacket surrounds the outer diameter of the stator lamination with a 50-50% ethylene glycol-water (WEG) coolant flowing through at various flow rates and inlet temperatures. On each axial end of the motor there are multiple jet nozzles, each of which delivers oil at flow rates and inlet temperatures. The jet fluid is issued into the end spaces inside the motor casing and then impinges onto the solid rotor end-windings and rotor lamination.

CFD analysis was conducted at different speeds, torques and inlet conditions. In this section, sample numerical results from CFD analysis are presented and discussed to prove the feasibility of the proposed design. Specifically, the focus is on the temperature distribution of the rotor and stator and the corresponding oil distribution within the motor. The boundary condition for these cases has been provided in the Table 4.2. Simulations involve splashing effects, various thermal resistances of the coil carrier, insulation paper, etc. Fig. 4.5 provides few pictures from CFD analysis.

Table 4.2. Boundary condition

ATF inlet temperature	65, 75 °C
WEG inlet temperature	65, 75 °C
Max. ATF volume flow rate	10 L/min
Max. WEG volume flow rate	10 L/min

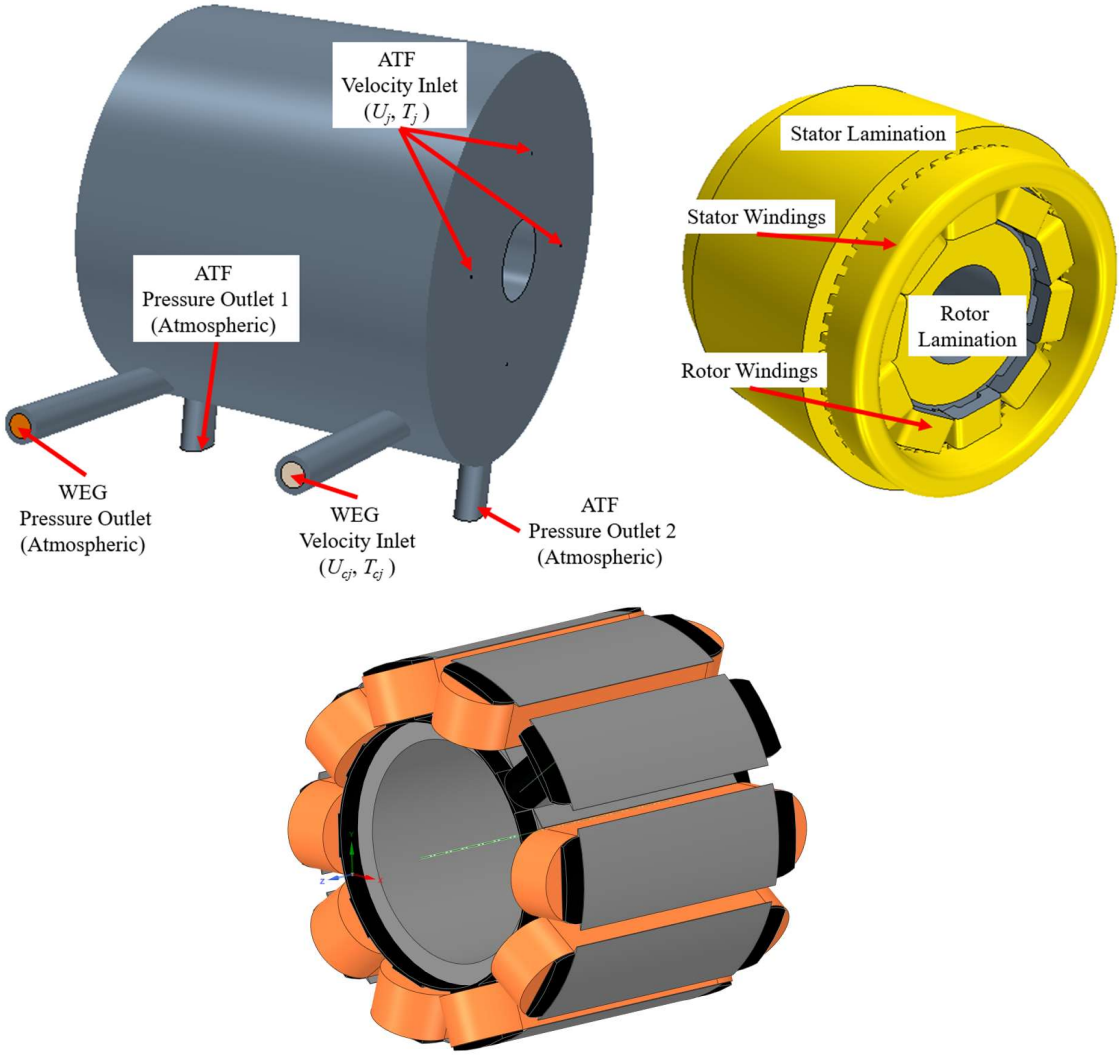

Fig. 4.4. Computational domains used for CFD and load distribution

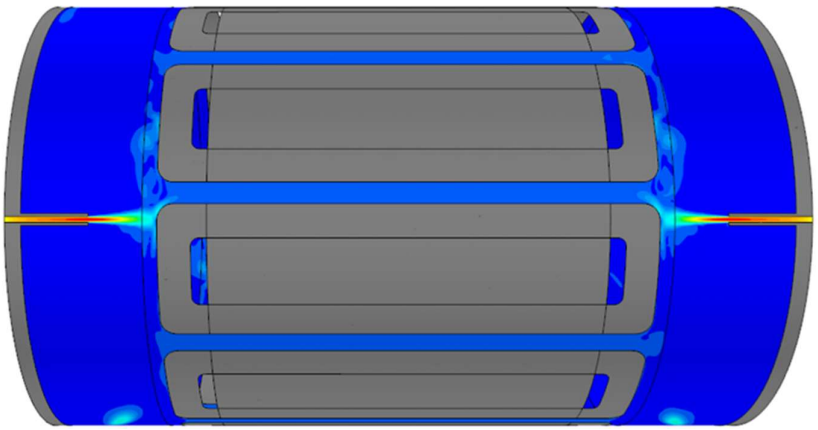

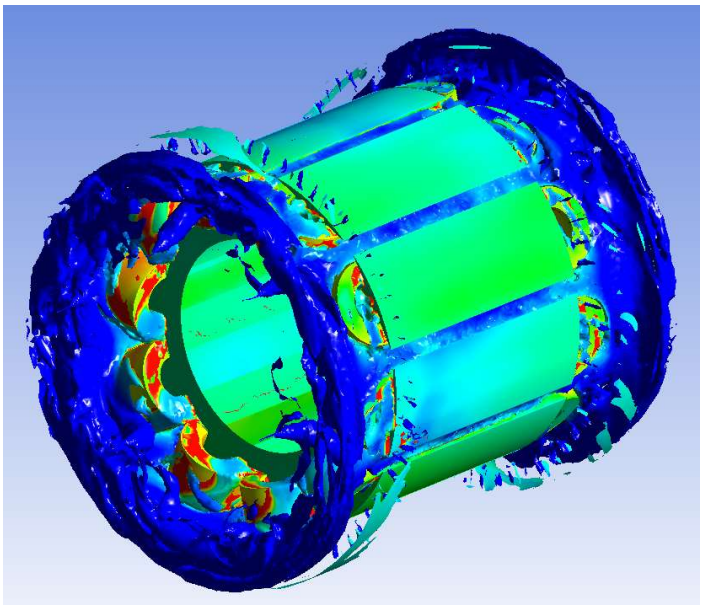

Fig. 4.5. Pictures from CFD simulations.

Figure 4.6 shows the temperature distribution for 500 rpm rotational speed. There is a slight 10°C decrement for the case with 65°C inlet temperature in comparison to 75°C. The rotor temperature is higher than the stator in terms of both average and maximum temperature. As it is depicted here, the hot spot is located in the middle of the rotor winding where there is low amount of oil. On the other hand, the rotor end windings can benefit from more fresh oil and therefore have lower temperature. For the stator, the temperature on the rear side of the windings is higher than the front side due the insulation material around the windings on the front side. Here, the stator lamination takes the most benefit of the WEG cooling jacket since it is surrounded by the WEG cooling jacket and has the minimum distance with it in comparison to the stator windings.

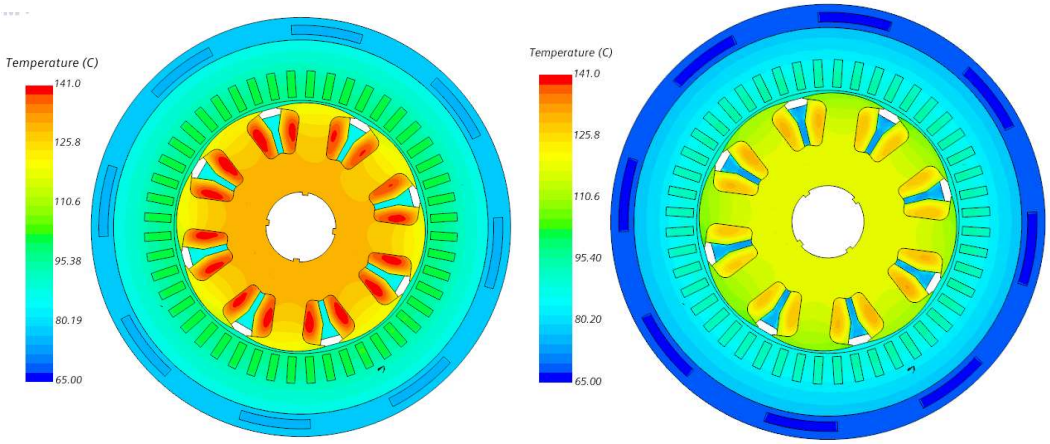

Coolant Inlet Temperature = 75°C Coolant Inlet Temperature = 65°C

Fig. 4.6. Temperature distribution for a rotational speed of 500 rpm

At this rotational speed, the fresh oil coming from the nozzle has the chance to touch the rotor end windings directly and take efficiently remove heat from it. As it is shown from the rotor cross section in Fig. 4.7, although the oil from the axil jet bends, it is still able to impinge the rotor windings located in front of this nozzle. Approximately 10% of the volume inside the motor housing is oil for this case. It is also clear that there is more oil near bottom of the motor in comparison to the top and the reason is lower rotational speed and greater effect of gravity.

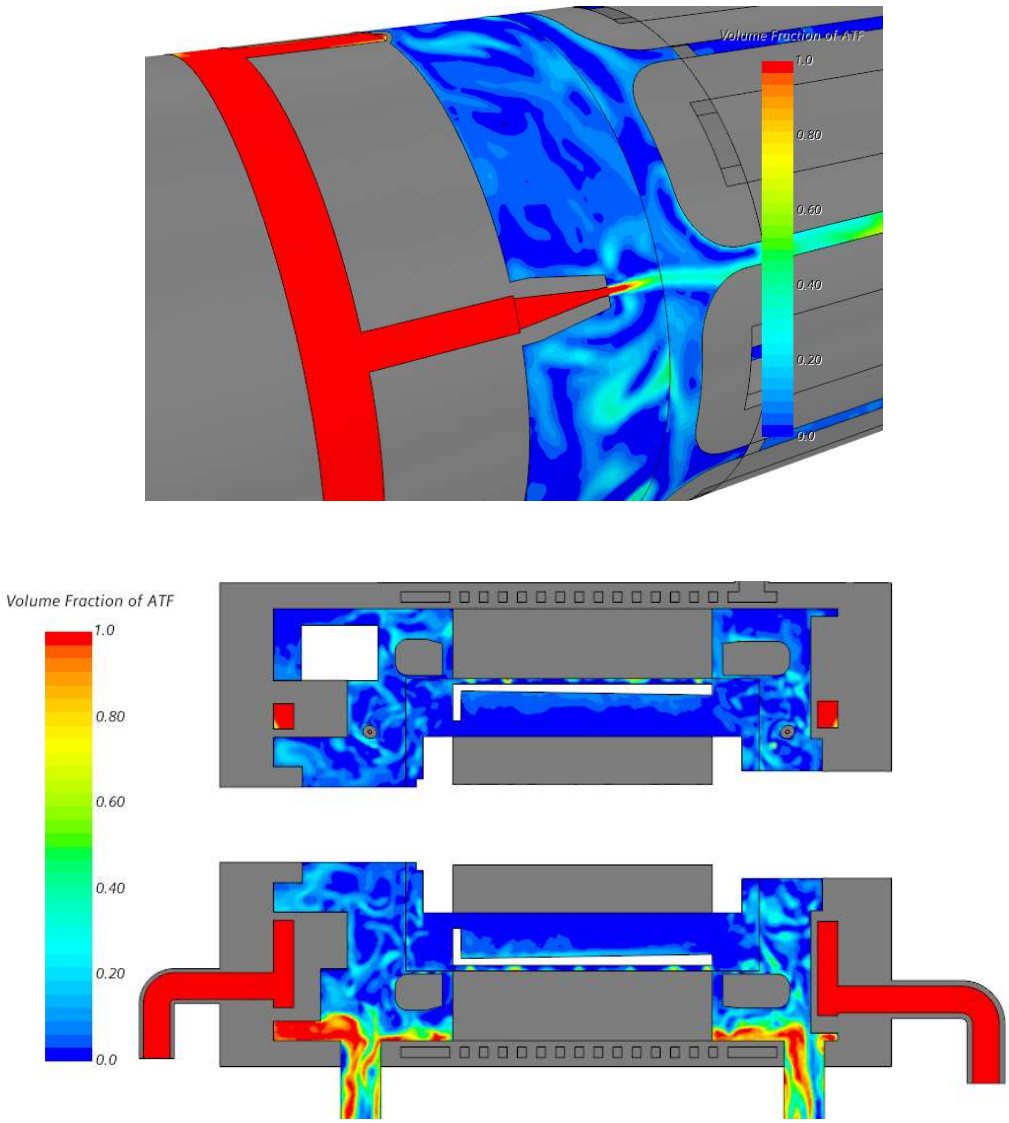

Fig. 4.7. Oil distribution for a rotational speed of 500 rpm

As shown in Fig. 4.8, the temperature for the rotor is lower at 4,455 rpm in comparison to the previous case at 500 rpm. Here the maximum temperature is also located in the middle or active region of the rotor winding due to the low amount of oil in this region. The temperature is lower for the rotor end windings in comparison to other location of the rotor and overall, in terms of temperature, there is a better cooling using an oil inlet temperature of 65°C in comparison to 75°C.

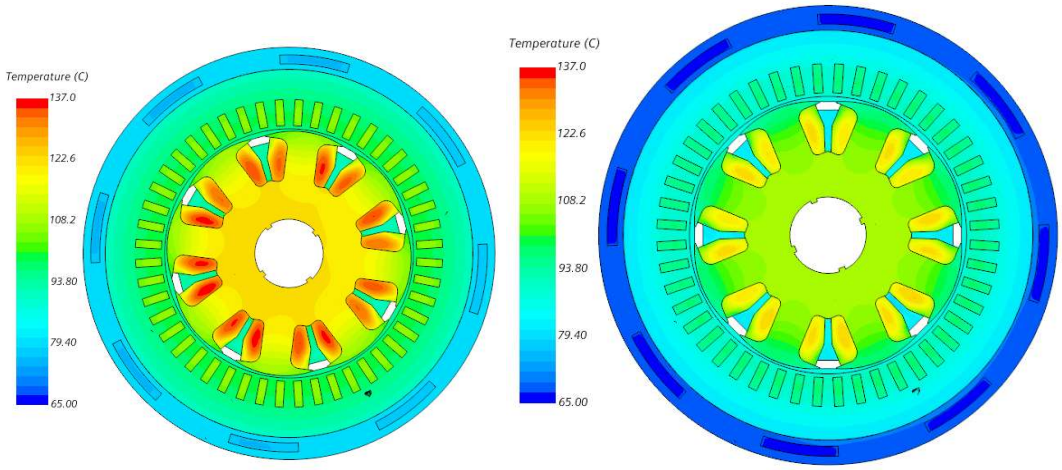

Coolant Inlet Temperature = 75°C Coolant Inlet Temperature = 65°C

Fig. 4.8. Temperature distribution for a rotational speed of 4455 rpm

From the CFD analysis conducted above it could be concluded that the proposed design could keep the motor cool below the target temperatures under all load points.

5. PROTOTYPE TESTING AND VALIDATION

Following the WFSM prototype development, further steps towards prototype testing and validation are stated below and explained in this section:

(i) Design of baseplate and coupling arrangement to test the WFSM on the dynamometer test bench.
(ii) Commissioning of stator inverter and rotor excitation inverter/constant DC supply.
(iii) Cooling system and control system setup
(iv) Comprehensive testing of the prototype WFSM system
(v) Data acquisition and analysis

After the prototype is built, as shown in Fig. 5.1 (a) & (b), further developments are made to allow precise mounting of the prototype on the dynamometer and are explained in brief in the following sections. This includes designing and developing a custom mounting plate, coupling adapter, support plate, and cooling inlet/outlets.

(a) (b)

Fig. 5.1. Built prototype before testing (a) drive end side, (b) non-drive end side.

Based on the measurements from the CAD design, a custom mounting plate is designed and developed, as shown in Fig. 5.2. This custom mounting plate ensures to hold the drive end side (DE) of the prototype to the flange plate of the dynamometer. The four holes on the mounting plate surrounding the void in the middle will help the prototype lock with the flange plate. The DE side shaft passes through the void of the mounting plate and will be coupled with the dynamometer. Additional holes are made surrounding the void to allow access to the cooling and thermocouples connections.

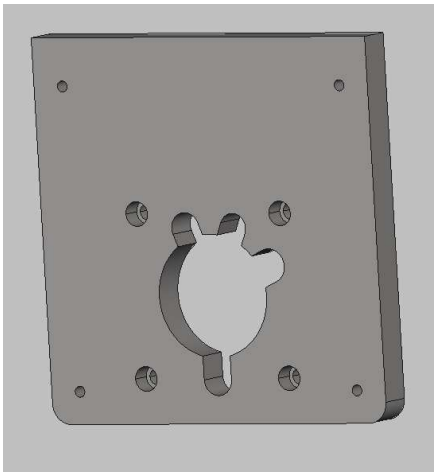

Fig. 5.2. Custom-built mounting plate.

A custom shaft coupler is designed based on the dimensions of the dynamometer and the WFSM shaft. As shown in Fig. 5.3, a coupler key is used between the shaft and the coupler, preventing the shaft from slipping. The coupler key is withheld by screws present on the coupler. Further, the coupling is completed after the shaft alignment, as shown in Fig. 5.4.

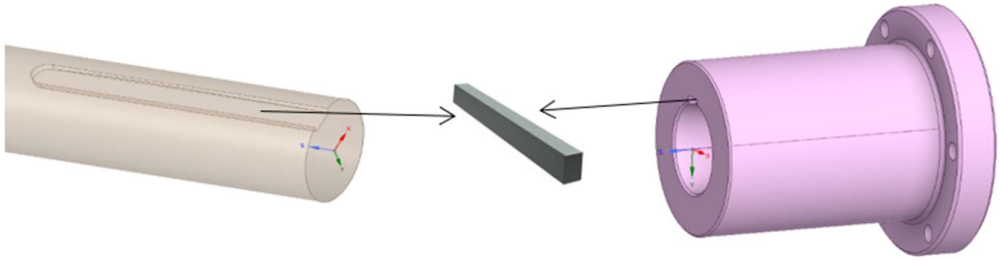

Fig. 5.3. Custom-built coupler with key for prototype shaft

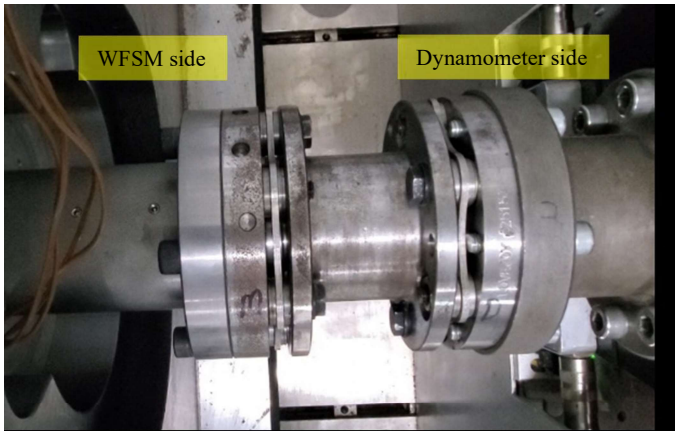

Fig. 5.4. WFSM prototype connected to dynamometer with custom-built coupler.

Using the analog level indicator shown in Fig. 5.5, the shaft alignment test is performed manually around the shaft. In case of any deflections in the alignment, metal shims, such as

0.05 mm, 0.25 mm, etc., are used underneath the mounting to adjust the alignment. Similarly, the prototype is also precisely adjusted perpendicular to the shaft for alignment.

Fig. 5.5. Analog level indicator for shaft alignment.

For the sake of mechanical stability and safer testing of the prototype on a dynamometer, a custom-built support plate is designed and built using the prototype CAD model again. The support plate is mounted on the bottom of the dynamometer flange plate and tightened to the housing on the Non-Driving-End (NDE) side as shown in Fig. 5.6.

Fig. 5.6. Custom-built support plate attached to the prototype on the test bench.

The built prototype has both oil and Water Ethylene Glycol (WEG) for cooling both the stator and rotor. As seen in Fig. 5.7, several L-shaped connectors are fitted to the prototype allowing the cooling pipes to be connected. Two L-shaped connectors are connected beneath the motor for the coolant outlet. The oil inlets to the jets are placed on both the NDE and the DE sides of the prototype. These jets are placed in this particular location after several simulations and investigations on their location, nozzle dimensions, spacing, etc. These inlets and outlets are used for rotor cooling i.e., using oil as the coolant. On the other hand, two L-shaped connectors are connected to the housing of the prototype stator cooling i.e., using WEG as the coolant for the stator jacket.

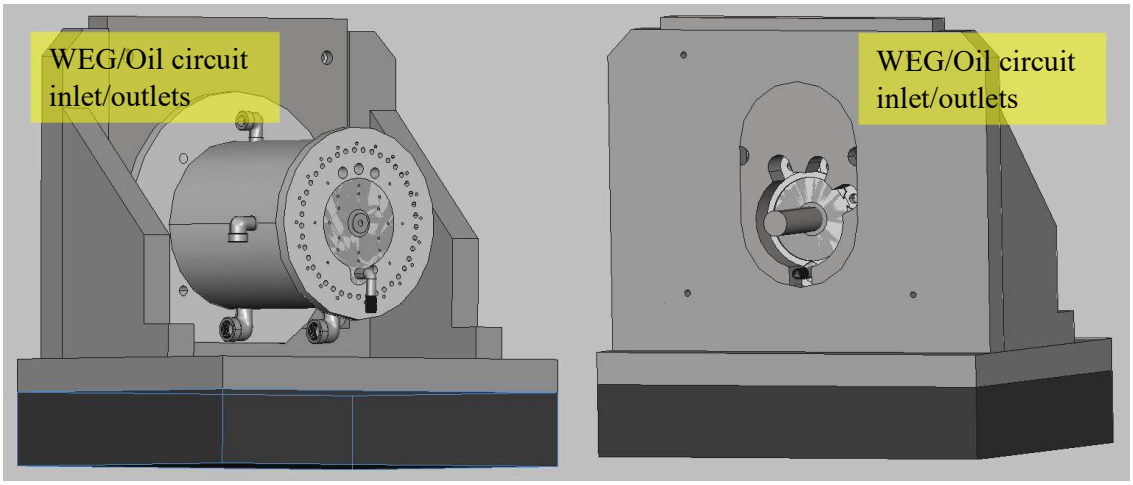

Fig. 5.7. Cooling inlet/outlet connectors installed on the prototype.

As shown in a schematic of the experimental setup in Fig. 5.8, the motor is mounted onto a dynamometer which controls the speed and losses to the motor. Two tanks hold and the two working fluids, WEG and oil. A built-in heat exchanger controls the temperature of the oil and WEG tanks which are approximately equal to the inlet temperatures of the two cooling circuits. Two control valves are used to control the flow rate of WEG (Valve #1) and oil (Valve #2) which is read using two flow meters. A magnetic inductive flowmeter is used to measure the flow rate of WEG and an oil flowmeter measures the flow rate of oil. To avoid clogging of the jet nozzles, a filter is installed after the flowmeter on the oil cooling circuit which will remove any impurities in the oil that can lead to clogging. Inlet and outlet temperatures of both cooling circuits are measured using K-type thermocouples installed after the flowmeters. Before the inlets of the cooling circuits, high pressure sensors are installed and after the outlets of each cooling circuit, low pressure sensors are installed. The difference between the high and low pressure readings of each cooling circuit is read by a digital pressure transducer.

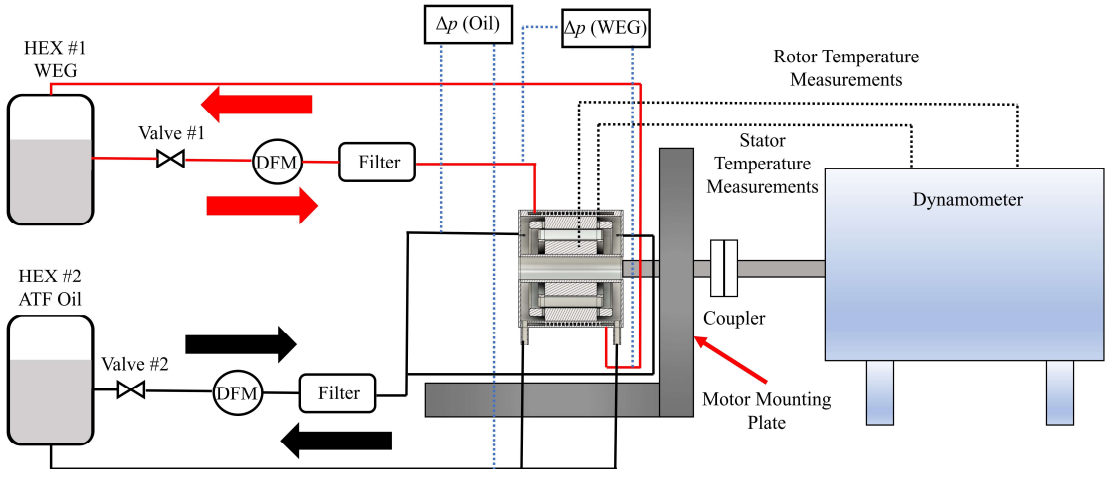

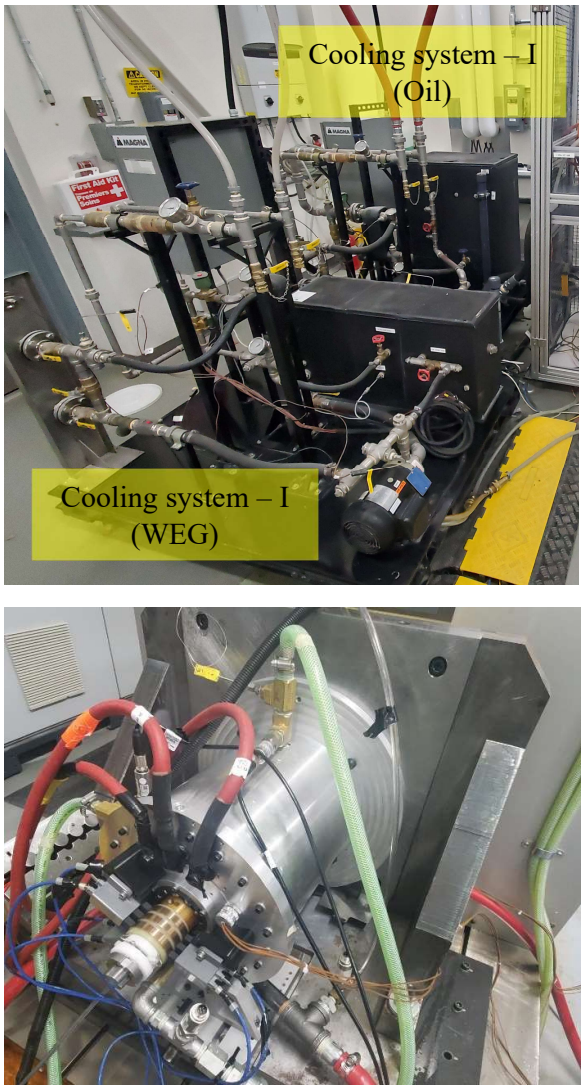

Fig. 5.8. Schematic of the cooling system set-up and connection to the motor

A three-phase IGBT inverter is used for the stator supply. As seen in Fig. 5.9, the inverter is attached with coolant pipes on either side and is cooled with WEG. The input for the inverter is supplied from a 600V DC bus simulator and the three-phase output is passed through the current sensors for the stator's current feedback. The PWM gate signals from the real-time controller are connected to the gate driver input of the inverter. The coolant is maintained at a flow rate of 10 LPM and the set temperature is fixed between -40^{O}C to 65^{O}C.

For the rotor constant DC supply, a three-phase SiC inverter is operated as a buck converter. The DC bus between the three-phase stator inverter and the rotor converter is shared. As seen in Fig. 5.10, the converter is also cooled by the WEG circuit. The flow rate is set to 12 LPM. The buck converter is controlled by the PWM gate signal generated from the real-time controller.

A four-channel power analyzer as shown in Fig. 5.11 is used for all the input measurements. Phase A is connected to the first channel and the following phases are connected

as shown in the figure. The fourth channel is allocated for the field winding. All four channels read respective voltage, current, power factor, etc, and are continuously logged into a spreadsheet. To calculate the efficiency, the speed and torque signals are connected to the power analyzer.

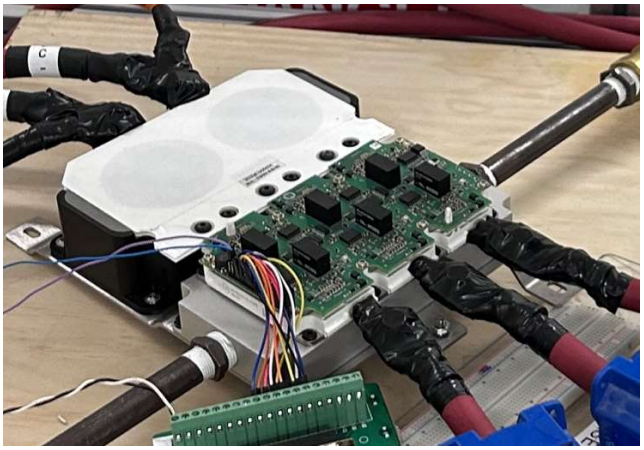

Fig. 5.9. Three-phase stator inverter connected to the prototype.

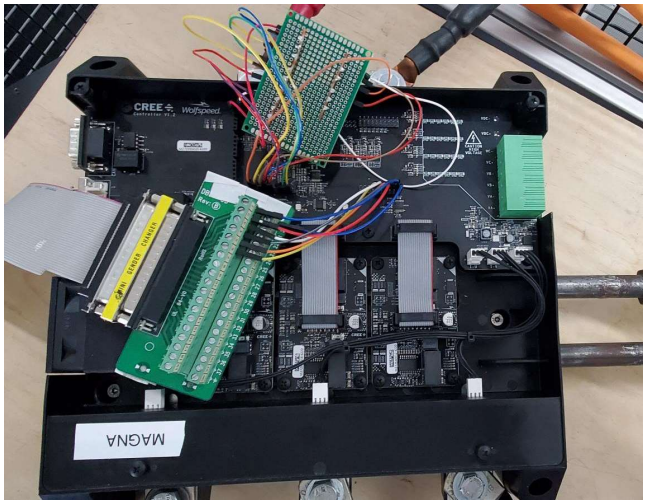

Fig. 5.10. Three-inverter operated as buck converter for WFSM field excitation.

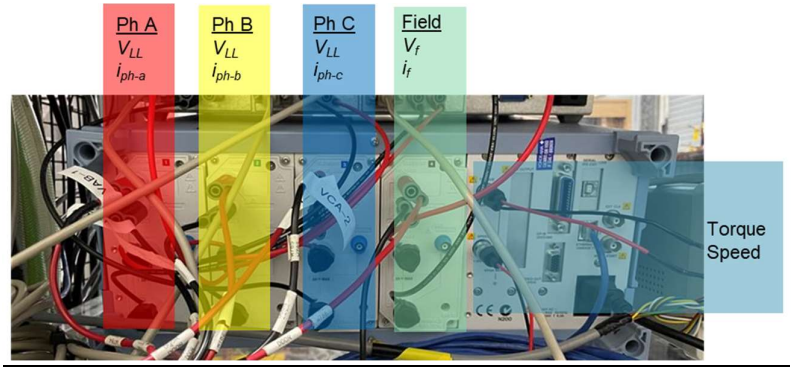

Fig. 5.11. Power analyzer with corresponding connections.

A differential pressure sensor is attached to both the oil and WEG cooling circuits as shown in Fig. 5.12 (a). The differential pressure sensors have a high side and a low side; where the high side is connected to the inlet side and the low side is connected to the output side of the motor. To measure the flow rate of both oil and WEG, multiple flow meters as shown in Fig. 3.11 (b), are connected to the respective cooling circuits both on the inlet and outlet sides.

(a) (b)

Fig. 5.12. (a) Differential pressure sensor, (b) analog flow meter.

During the development stage of the prototype, several thermocouples are placed at various locations around the stator windings. All the thermocouples are of K-type and are connected to an 8-channel temperature measure unit module. The temperature measurements are continuously logged into the chart recorder. Similarly, the temperatures of the cooling fluids including WEG/oil are also measured on another thermal DAQ.

After the successful completion of the installation of the prototype on the dynamometer, a few static tests are performed such as stator inverter and rotor inverter testing with loads, resolver position feedback test, resistance tests, cooling circuits test, position feedback test, etc. The following sections explain the conducted tests.

With the help of a current control source, a known amount of current is passed through the stator/rotor windings for resistance measurement. Using a precise multimeter as shown in Fig. 5.13, the DC current and the voltage across the windings are measured. Using Ohm's law i.e., $V=IR$, the resistance is calculated through the measured voltage and current. Calculation adjustments are made as per the type of stator windings configuration, i.e., star configuration or delta configuration. At a given recorded room temperature, the test is performed at various current levels and an average of resistances is taken for the record final recording.

Fig. 5.13. High precision multimeter used for the resistance test.

The resolver position feedback test is performed as the rotor position is crucial for the closed-loop control system. A sinusoidal wave excitation at a given amplitude and frequency as per the datasheet is provided to the excitation terminals of the resolver. The excitation signal was generated by the real-time controller's analog output. The output of the resolver i.e., sin and cos signals are read into the controller via analog input terminals. The rotor position is calculated by solving the sin/cos signals read. The rotor was rotated at a constant speed by the dynamometer to test the resolver by providing the excitation signal. Fig. 5.14 shows a sample resolver position output when the rotor is rotated at a constant speed. As seen in the figure, the rotor position signal is a sawtooth waveform ranging from (0, 360) deg.

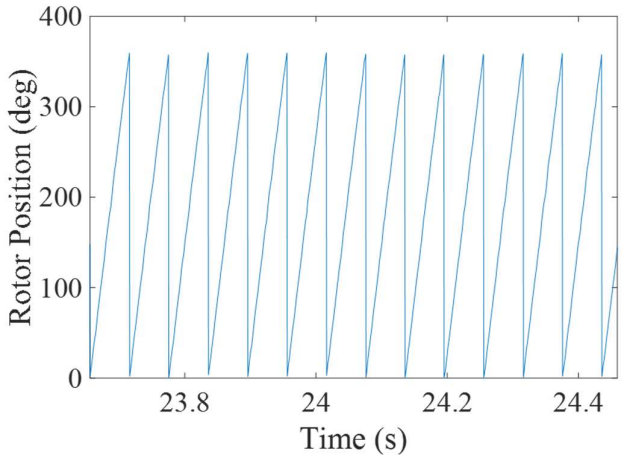

Fig. 5.14. Rotor position output (deg) when rotated at a constant speed.

The brush loss test is performed to calculate the amount of voltage dropped across the brush due to its resistance. It can be seen that the brushes are in series with field windings as shown in the equivalent circuit diagram of the field circuit in Fig. 5.15. A constant DC field supply is applied on positive and negative terminals of the brushes, where the field current passes through the brushes and field winding. At various field currents, the DC field voltage (V_{Supply}) and voltage across the field winding (V_{Field}) are measured. The V_{Field} is measured across the slip-rings of the rotor. It is assumed that the voltage across the slip-ring terminals is equal to the voltage across the field winding terminal. Hence, using the formula $V_{Supply} = V_{Brush} + V_{Field}$, the V_{Brush} can be estimated.

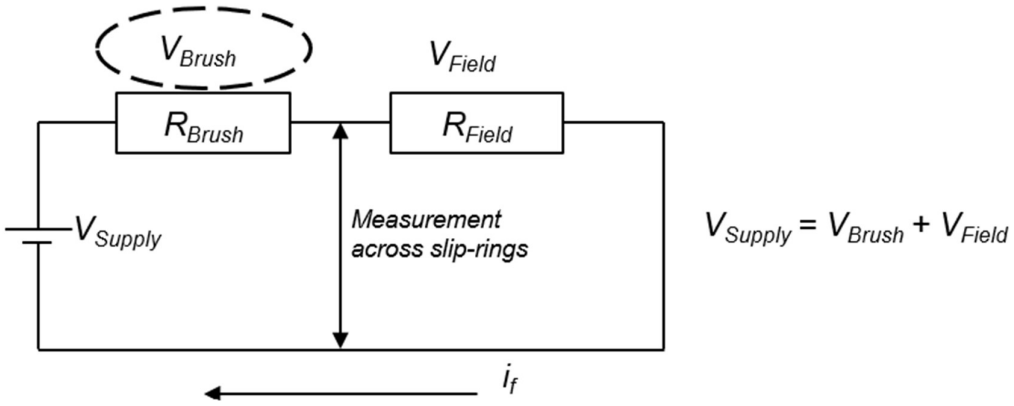

Fig. 5.15. Equivalent circuit diagram of brushes and field winding.

Maintaining the exact flow rate and set temperature of the coolant for both the WEG/oil cooling circuits are important during the tests. Hence, cooling circuit tests are performed individually on both WEG/oil circuits. Various flow rates are tested on the flow meter by regulating the valve of the cooling circuit pump. With various set flow rates, the pressure difference is measured at the inlet and outlet of the motor to make sure that there are no blocks in the cooling circuit due to any impurities in the cooling circuit. Fig. 3.16 shows the oil returning to the tank during the test. The heating rod immersed in the tank for regulating temperature can also be seen in the figure.

Fig. 5.16. Oil outlet flowing into the tank.

Before the steady state tests, the stator inverter functionality is tested with the inductive load. The main aim of this test is to verify the SPWM gate signals generated from the real-time controller, SPWM dead-time, gate driver circuit, current sensors, and the three-phase stator inverter when connected to the load. As shown in Fig. 5.17 (a), the three-phase stator inverter is supplied by a DC supply, and the three-phase output is connected to an L load. The wires are also passed through three current sensors for measurement. The three current sensors are read into the real-time controller through analog input terminals. This measurement is again verified against the load current measurement read from an external oscilloscope as shown in the figure. The SPWM gate signals from the controller are amplified by an external gain circuit and then are connected to the inverter gate driver input. During this test, the inverter is cooled by a WEG chiller at a set flow rate and temperature. The test is performed in an open-loop without any feedback control, the stator inverter and other component functionality are verified at various modulation indexes and control frequencies. A sample three-phase sinusoidal three-phase current during the test is shown in Fig. 5.17 (b).

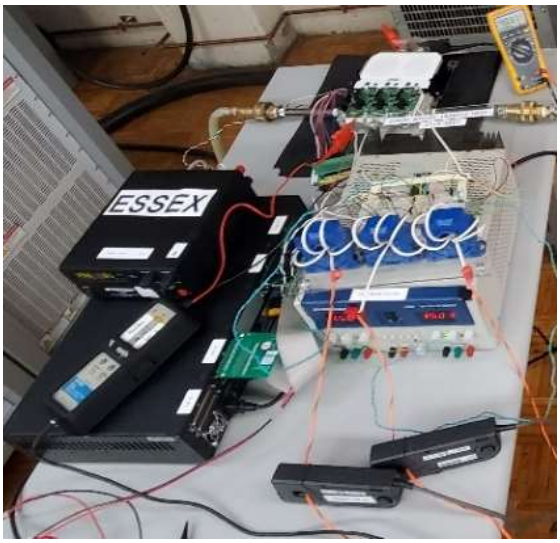

(a)

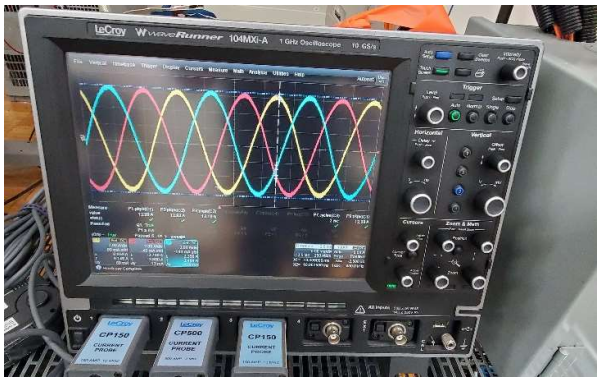

(b)

Fig. 5.17. (a) Three-phase stator inverter connected to L load for open-loop testing, (b) three-phase sinusoidal load currents.

Similar to the stator inverter test, the rotor converter i.e., inverter operated as a buck converter is also tested by connecting a RL load. The main goal of this test is to verify the functionality of the rotor converter, PWM signals, gate driver circuit, current sensor, etc. As seen in Fig. 5.18 (a), the rotor converter is supplied by the DC supply, and the output from one of the three-phase and negative of the DC input is connected across an RL load. The wires are also passed through a current sensor that is read by the real-time controller. The current sensor functionality is again verified by an external oscilloscope measuring the same load current. During the test, the rotor converter temperature is regulated by a WEG chiller at a set flow rate and temperature. This test is performed in an open-loop condition. Hence, the measurements are taken at various PWM duty ratios and various RL loads. Fig. 5.18 (b), shows a sample output of voltage across the load and load current.

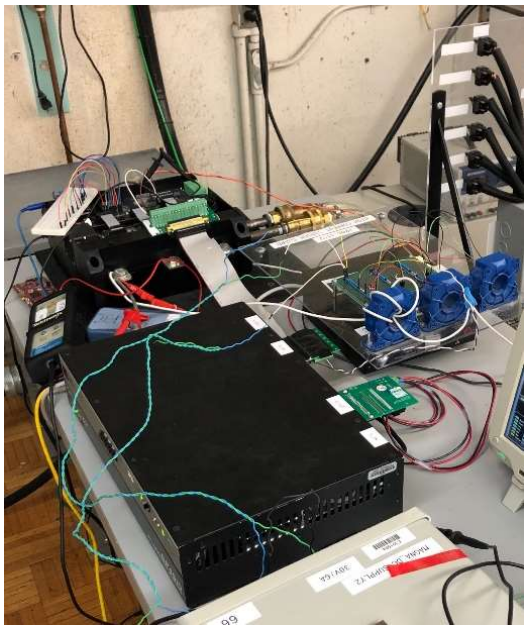

(a)

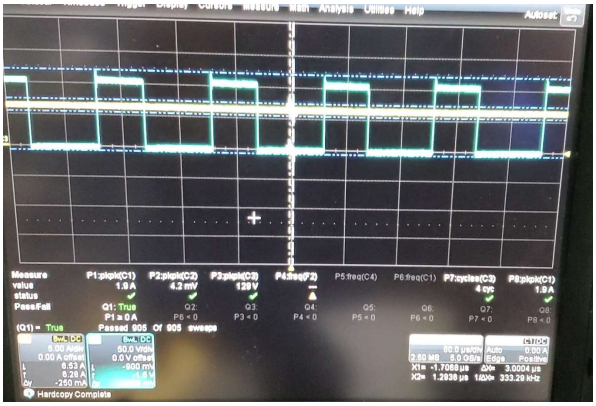

(b)

Fig. 5.18 (a) Rotor converter connected to an RL load for open loop testing, (b) load voltage and current at a given duty ratio.

The back-EMF test is performed to verify the experimental results with FEA results. After the rotor buck converter is tested with the RL load, the converter is then connected to the field winding of the prototype. The rotor winding is excited by a constant field current, and the rotor is rotated by the dynamometer at a constant speed for the back-EMF test. The line-line voltage at the stator terminals is measured. Fig. 5.19 (a) shows the recorded back-EMF line-line voltage at a field excitation current of 4A and a constant rotor speed of 1000 rpm. The experimental results are compared to the FEA result as shown in Fig. 5.19 (b). It can be seen that the experimental results closely match the FEA results. This comparison concludes that the windings of the built prototype closely match the motor design. The back-EMF test and the comparison against FEA results are further performed at various other speeds and field excitation currents.

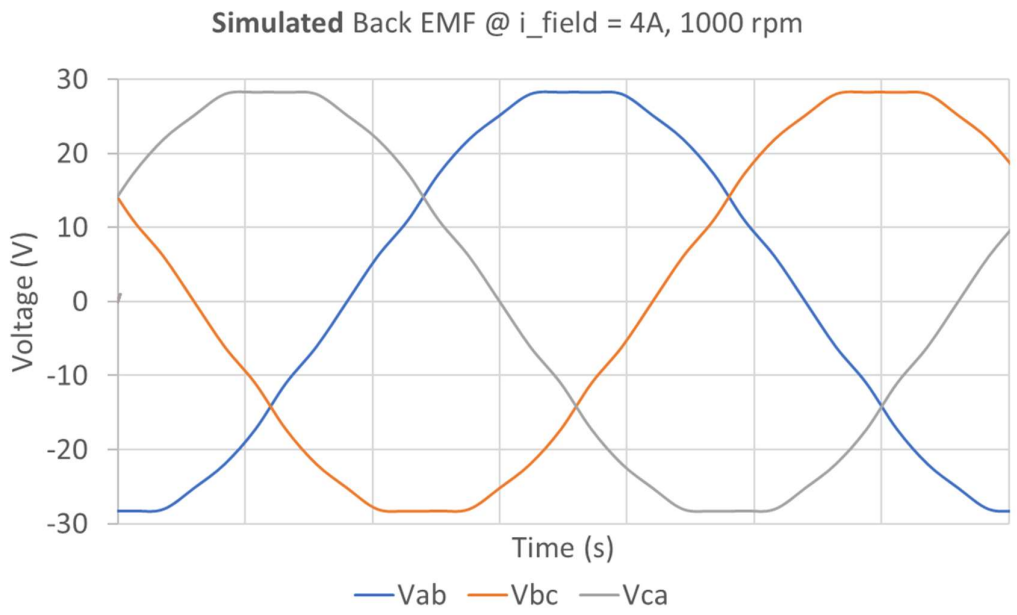

(a)

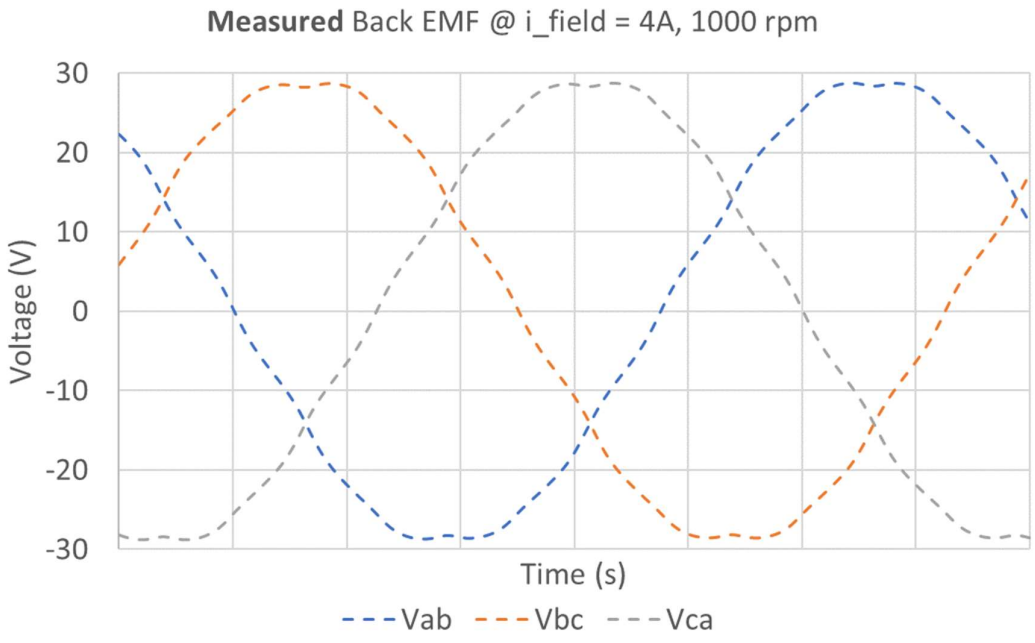

(b)

Fig. 5.19. (a) Simulated back-EMF at a field current of 4A and rotor speed of 1000 rpm, (b) Measured back-EMF at a field current of 4A and rotor speed of 1000 rpm.

In the previous section, several static tests were performed to verify various component functionality. Now, bringing everything together, a few of the load points were tested at steady-state for evaluating the performance of the built prototype and validating the developed models. The experimental results were compared with the FEA results. The steady-state tests were carried out for a longer amount of time allowing the temperature of the stator, rotor, and WEG/oil coolant temperatures to attain equilibrium temperatures. Closed-loop current control model is used for steady-state testing.

The complete block diagram of the developed control model is shown in Fig. 5.20. The control model is developed in the rotor reference *dq* frame. This is done for more straightforward implementation and controllability. As seen in the block diagram, the stator and rotor currents are controlled separately in their respective closed loops. Both the closed loops are developed based on Proportional-Integral (PI) controller strategy. The feedback for the closed-loop control loops is from sensors, namely: (i) three-stator current sensors, (ii) rotor field current sensor, and (iii) position feedback sensor.

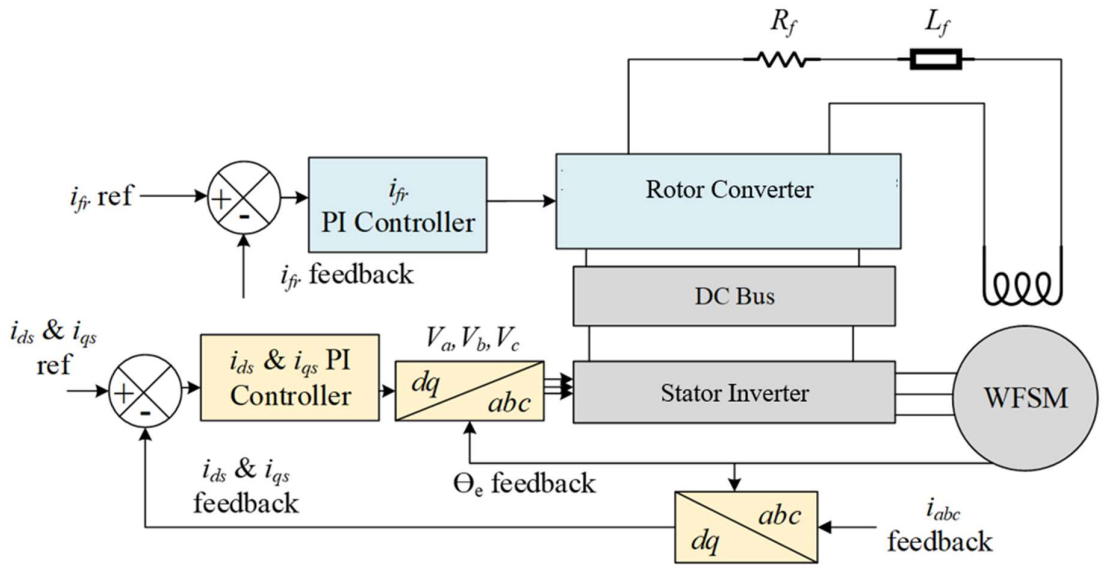

Fig. 5.20. Developed closed-loop current control model.

Fig. 5.21 shows the software model developed and its interface with the hardware. The software model is developed in a real-time RCP/HIL system as shown in Fig. 5.22. The control model mentioned above is developed in MATLAB/SIMULINK to run in RCP mode inside the real-time system. This controller uses an INTEL multicore 3.5 GHz processor with Xilinx Kintex 7 FPGA. The 128 fast I/O includes 16 analog output, 16 analog input, 32 digital output, and 32 digital input channels. The Analog In (AI) ports read all the sensor inputs into the real-time system. The Digital Out (DO) sends the PWM gate signal to the gate drivers of both the stator inverter and rotor converter. The whole control loop runs in the fixed time step mode to ensure synchronism.

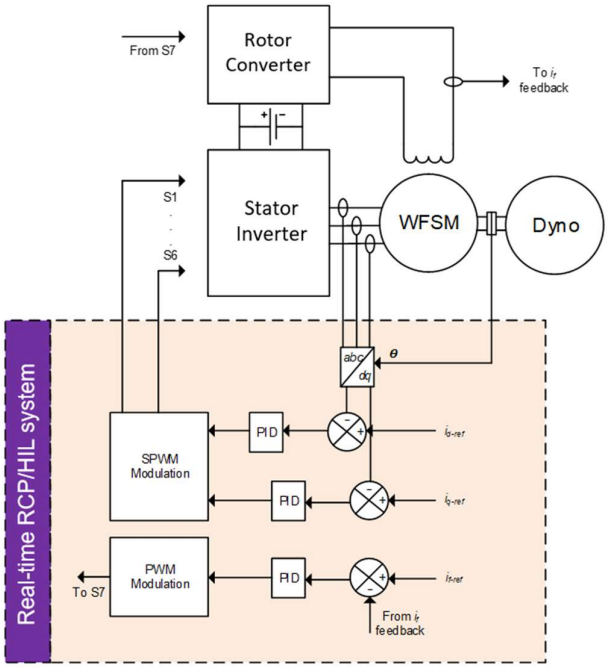

Fig. 5.21. Developed software model interfacing with hardware.

Fig. 5.22. Real-time RCP/HIL controller

Table 5.1:

Load Point 1		
	Simulation Data	**Experimental Data**
Speed (rpm)	4455	4455
Torque (Nm)	120.09	118.11
i_d **(A)**	-55.91	-55.90
i_q **(A)**	346.06	346
i_{abc_pk} **(A)**	350.55	341.12

i_f **(A)**	12.80	12.97
V_{DC} **bus (V)**	325	325

Table 5.2:

Load Point 2		
	Simulation Data	**Experimental Data**
Speed (rpm)	500	500
Torque (Nm)	352.20	351.53
i_d **(A)**	-251.83	-251
i_q **(A)**	860.88	860
i_{abc_pk} **(A)**	896.96	894
i_f **(A)**	28.10	28.10
V_{DC} **bus (V)**	325	325

Table 5.3:

Load Point 3		
	Simulation Data	**Experimental Data**
Speed (rpm)	5549	5548
Torque (Nm)	26.94	23.33
i_d **(A)**	2.08	2.07
i_q **(A)**	111.31	111.31
i_{abc_pk} **(A)**	111.33	108.14
i_f **(A)**	4.28	4.47
V_{DC} **bus (V)**	400	400

Out of many load points tested, table 5.1, 5.2, and 5.3 show some of the sample steady-state testing points. The torque and speed are used to calculate the output power of the machine and the three-phase currents are used to calculate the input power of the motor.

Fig. 5.23 shows a sample torque and speed profile over time, where the maximum torque achieved is ~ 350 Nm at a speed of 2753.55 rpm. This was achieved at a stator RMS current of 627.28 A and field current of 28.2 A as shown in Fig 5.24, 5.25.

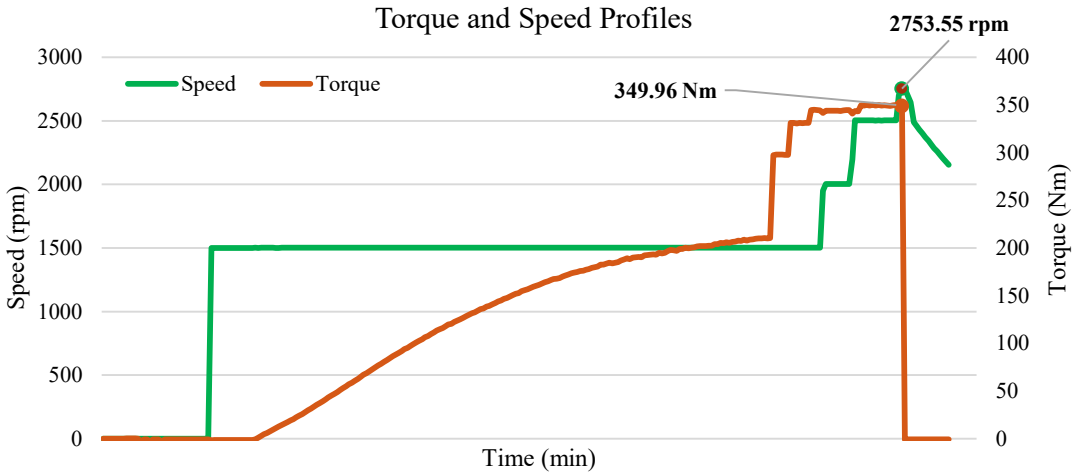

Fig. 5.23. Torque, speed vs. time profile during peak loading condition.

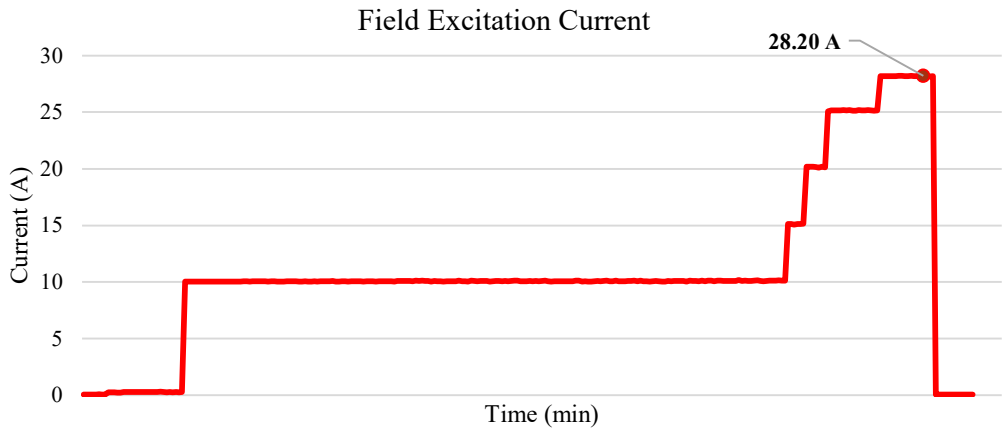

Fig. 5.24. Field excitation vs. time profile.

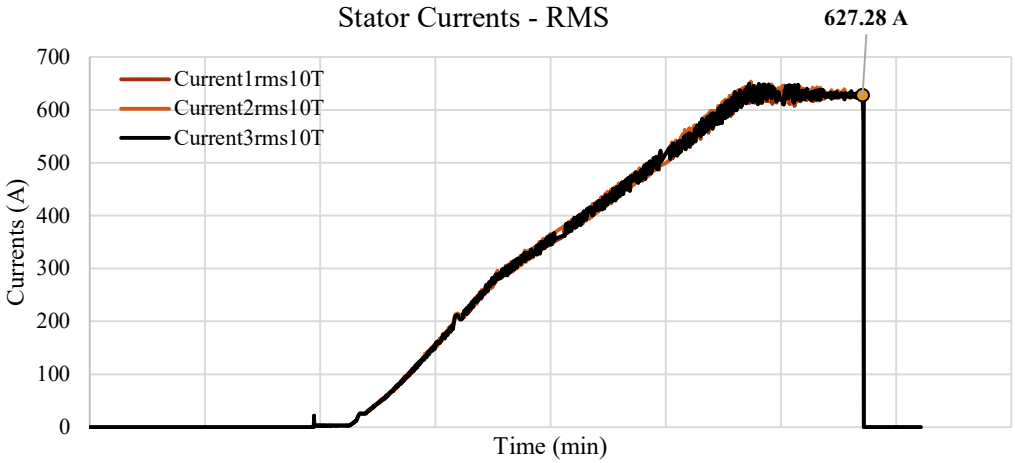

Fig. 5.25. Stator RMS current vs. time profile.

Following the design and prototyping of the high-power density WFSM, the necessary steps for setting up the test bench have been followed. These include developing software control models, various mechanical building blocks, cooling circuits, and electrical and measuring instruments. In the end, selected load points were tested at steady-state at given operating conditions. The experimental results obtained closely match the design FEA simulation data. Hence, it can be concluded that the machine was prototyped according to machine design requirements and the performance closely match with intended machine design performance. Along with the steady-state cluster load testing, several other static tests were also performed on the built prototype and other building blocks.

This concludes that:

- Selected motor design was optimized for manufacturing
- Various parts of the motor such as shaft, casing, stator jacket, etc. were designed for manufacturing and testing
- Various parts of the rotor excitation system such as cores, casing, rotating rectifier, etc. were designed for manufacturing and testing
- Test bench was developed with hardware and software for motor control and data acquisition
- Parts were ordered, received, assembled and prototype build was completed
- Developed motor model was validated at different speeds, maximum currents and torque.
- Measured and simulated results were matching closely at various load points
- Measurement and simulation results prove that the WFSM prototype can deliver 50kW/L and cost less than $3.3/kW

6. REFERENCES

1. J. K. Noland, S. Nuzzo, A. Tessarolo, and E. F. Alves, “Excitation system technologies for wound-field synchronous machines: Survey of solutions and evolving trends,” IEEE Access, vol. 7, pp. 109699–109718, 2019.
2. S. Hagen, M. Tisler, J. Dai, I. P. Brown and D. C. Ludois, "Use of the Rotating Rectifier Board as a Capacitive Power Coupler for Brushless Wound Field Synchronous Machines," in IEEE Journal of Emerging and Selected Topics in Power Electronics, vol. 10, no. 1, pp. 170-183, Feb. 2022, doi: 10.1109/JESTPE.2020.3039497.
3. S. Hagen, M. Tisler, J. Dai, I. P. Brown and D. C. Ludois, "Use of the Rotating Rectifier Board as a Capacitive Power Coupler for Brushless Wound Field Synchronous Machines," in IEEE Journal of Emerging and Selected Topics in Power Electronics, vol. 10, no. 1, pp. 170-183, Feb. 2022, doi: 10.1109/JESTPE.2020.3039497.
4. Liben, Marisa J. T. “Capacitive Power Transfer Field Excitation with an Integrated Resolver for Synchronous Machines,” Ph.D. Thesis, Electrical & Computer Engineering, University of Wisconsin – Madison, 2023.
5. D. C. Ludois, K. J. Frankforter, S. E. Behringer and F. A. Roberts, "Double Layer Capacitive Power and Heat Transfer in Rotating Machinery," in IEEE Transactions on Industry Applications, vol. 58, no. 5, pp. 6115-6124, Sept.-Oct. 2022, doi: 10.1109/TIA.2022.3184666.
6. McLyman, Colonel Wm. T. “Transformer and Inductor Design Handbook,” 4th Edition. CRC Press, 2011.
7. A. Boglietti, A. Cavagnino, D. Staton, M. Shanel, M. Mueller and C. Mejuto, "Evolution and Modern Approaches for Thermal Analysis of Electrical Machines," in IEEE Transactions on Industrial Electronics, vol. 56, no. 3, pp. 871-882, 2009.
8. E. Cousineau, K. Bennion, V. Chieduko, R. Lall and A. Gilbert, “Experimental Characterization and Modeling of Thermal Contact Resistance of Electric Machine Stator-to-Cooling Jacket Interface Under Interference Fit Loading,” *Journal of Thermal Science and Engineering Applications*, vol. 10, no. 4, pp. 1-7, 2018.
9. X. Yang, A. Fatemi, T. Nehl, L. Hao, W. Zeng and S. Parrish, "Comparative Study of Three Stator Cooling Jackets for Electric Machine of Mild Hybrid Vehicle," *2019 IEEE International Electric Machines & Drives Conference (IEMDC)*, San Diego, CA, USA, pp. 1202-1209, 2019.
10. E. Chen and G. Rupertus, "Development of Water Jacket Cooled Motor and its Applications in Cement Industry," *2017 IEEE-IAS/PCA Cement Industry Technical Conference*, Calgary, AB, Canada, pp. 1-18, 2017.
11. D. P. Kulkarni, G. Rupertus and E. Chen, "Experimental Investigation of Contact Resistance for Water Cooled Jacket for Electric Motors and Generators," *IEEE Transactions on Energy Conversion*, vol. 27, no. 1, pp. 204-210, 2012.
12. Y. Gai, M. Kimiabeigi, J. D. Widmer, Y. C. Chong, J. Goss, U. SanAndres and D. A. Staton, "Shaft Cooling and the Influence on the Electromagnetic Performance of Traction Motors," *2017 IEEE International Electric Machines and Drives Conference (IEMDC)*, Miami, FL, USA, pp. 1-6, 2017.
13. J. Nonneman, B. van der Sijpe, I. T'Jollyn, S. Vanhee, J. Druant and M. de Paepe, "Evaluation of High-Performance Rotor Cooling Techniques for Permanent Magnet

Electric Motors," *2021 IEEE International Electric Machines & Drives Conference (IEMDC)*, Hartford, CT, USA, pp. 1-7, 2021.
14. M. H. Park and S. C. Kim, “Thermal characteristics and Effects of Oil Spray Cooling on In-Wheel Motors in Electric Vehicles,” *Applied Thermal Engineering*, vol. 152, pp. 582-593, 2019.